

1 **Geophysical Trends inferred from 20 years of AIRS**  
2 **infrared global observations**

3 **S. DeSouza-Machado<sup>1</sup>, L. Larrabee Strow<sup>1,2</sup>, R. Kramer<sup>3</sup>**

4 <sup>1</sup>JCET/GESTAR2, University of Maryland Baltimore County, Baltimore, Maryland

5 <sup>2</sup>Dept of Physics, University of Maryland Baltimore County, Baltimore, Maryland

6 <sup>3</sup>NOAA GFDL, Princeton New Jersey

7 **Key Points:**

- 8 • The 20+ year low noise high spectral radiance record by NASA's Atmospheric In-  
9 frared Sounder contains detailed vertical information about surface and atmospheric  
10 temperature and water vapor.
- 11 • Trends from the radiance measurements are analyzed in a novel way for long-term  
12 climate studies, different than traditional use of infrared radiances in daily retrievals  
13 or assimilation into Numerical Weather Prediction Models.

---

Corresponding author: Sergio DeSouza-Machado, [sergio@umbc.edu](mailto:sergio@umbc.edu)

**Abstract**

NASA's Atmospheric Infrared Sounder has been in near-continuous operation since September 2002. The  $\sim 3$  million daily spectral observations contain detailed information about surface and atmospheric temperature, water vapor and trace gases such as CO<sub>2</sub> and CH<sub>4</sub>, as well as clouds and aerosols. In this paper we obtain climate thermodynamic trends using 20 years of AIRS observations by working exclusively with the trends observed in the AIRS radiance time series. This is achieved by first binning the observed spectra into nominal  $3 \times 5$  degree latitude/longitude spatial subsets using 16 day intervals, after which a quantile-based algorithm selects nominally clear scenes for each grid box in order to construct the clear scene radiance spectrum time series. De-seasonalized spectral anomalies and spectral trends are then obtained from the time series, which are converted into geophysical trends using a physical retrieval for each grid box. This approach is completely different from traditional operational use of infrared data for trending, whereby anomalies/trends are generated either after daily retrievals, or after assimilation into NWP models. Our approach rigorously ties the derived geophysical trends to the observed radiance trends, and requires orders-of-magnitude fewer computational resources and time than re-analysis or traditional Level 2 retrievals. The retrieved trends are compared to trends derived from four other products : ERA5, MERRA2 reanalysis model fields and the NASA Level3 AIRS v7 and NASA Level 3 CLIMCAPS v2. Our retrieved surface temperature trends agree quite well with ERA5 re-analysis, CLIMCAPS L3 and the GISS surface climatology trends. Atmospheric temperature profile trends exhibit some variability amongst all these data sets, especially in the polar stratosphere. Water vapor profile trends are nominally similar amongst all data sets except for the AIRS v7 which exhibits trends with a different sign in the mid troposphere. Spectral closure between observation trends versus those computed by running all the NWP re-analysis and official NASA L3 monthly fields though a (clear sky) radiative transfer code is discussed, with the major differences arising in the water vapor sounding region.

**Plain Language Summary**

The new generation of infrared sounders, designed for weather forecasting purposes, have been in orbit around the Earth for a long enough time to enable anomaly and trending studies for climate purposes. Traditionally their daily obtained radiance data has been used for operational atmospheric state retrievals, or assimilation into Numerical Weather Prediction models, after which climate anomaly studies are made. In this paper we use the raw radiance spectral data to form radiance anomalies and trends, after which we do a one step atmospheric state retrieval. This novel approach has the benefit of using only stable channels together with easily understood assumptions and well tested retrieval algorithms to do the trend or anomaly geophysical retrieval, which has full error characterization.

**1 Introduction**

NASA's Atmospheric Infrared Sounder (AIRS) became operational in September 2002, as the first of the new generation of low noise, high stability hyperspectral sounders, making Top of Atmosphere (TOA) radiance observations at a typical 15km (at nadir) horizontal resolution. Follow on instruments with similar characteristics and abilities include Eumetsat's Infrared Atmospheric Sounding Interferometer (IASI) and NOAA's Cross Track Infrared Sounder (CrIS), operational since June 2007 and March 2012 respectively. The latter two already have follow on missions planned till the 2040s, and together these three sounders will provide scientists with a 40 year high quality, near continuous observational dataset for climate anomaly and trending studies.

Infrared radiances contain a wealth of information, including but not limited to surface temperature, atmospheric temperature and water amount, and mixing ratios of green-

64 house gases such as carbon dioxide CO<sub>2</sub>, CH<sub>4</sub> and N<sub>2</sub>O. Measurements by visible im-  
 65 agers which have  $\sim 1$  km horizontal resolution or better King et al. (2013) suggest global  
 66 cloud free fractions of  $\sim 30\%$ , but the 15 km footprint of typical sounders means at most  
 67 5% of the hyperspectral observations can be considered “cloud-free.” Current operational  
 68 NASA L2 products use the method of cloud clearing on observed radiances in partly cloudy  
 69 scene conditions before doing the geophysical retrieval. The cloud clearing method solves  
 70 for an estimate of clear column radiances by examining adjacent Fields of View (FOVs)  
 71 to estimate the cloud effects on observed allsky radiances, assuming any differences are  
 72 solely due to different cloud amounts in each FOV, and significantly increases geophys-  
 73 ical retrieval yields (to about 50-60%) Smith and Barnett (2023). This does introduce in-  
 74 creased noise in the cloud cleared radiances of the lower atmosphere sounding channels;  
 75 in addition the subsequent retrieval depends on the first guess (which is a neural net for  
 76 AIRS v7 and MERRA2 reanalysis for CLIMCAPS v2). The reader is referred to Susskind  
 77 et al. (2003); Smith and Barnett (2020, 2023) for more details.

78 In this paper we work directly in radiance space and form either anomalies or trends  
 79 from the underlying well characterized and understood radiances Strow and DeSouza-  
 80 Machado (2020), in order to do a geophysical trend or anomaly retrieval. The work pre-  
 81 sented here, once the averaged/sorted data is available, can be processed in hours to days,  
 82 and can be duplicated by small research groups with ease. Moreover, our novel approach  
 83 has zero temperature *a-priori* and minimal water vapor *a-priori*. This completely sidesteps  
 84 time variability and the accuracy of the *a-priori* which causes errors in the retrievals,  
 85 and ensures our work examines trends directly inferred from the radiances versus those  
 86 from traditional methods. This leads to more unbiased results that directly highlight the  
 87 conditions (for example stratospheric water vapor) where the sensor has limited sensi-  
 88 tivity.

89 The approaches used in this work are therefore very different than climate anoma-  
 90 lies or trends from reanalysis products or traditional Level 2 retrievals, neither of which  
 91 are tailored for climate trends. Reanalysis products assimilate individual sensor scenes  
 92 from many different instruments, and may have discontinuities as different instruments  
 93 come online or go offline. Traditional Level 2 (and Level 3 products derived from Level  
 94 2) retrieve the atmospheric state for individual scenes (or effective cloud-cleared radi-  
 95 ance derived from a 3x3 grid of individual scenes). Both reanalysis and Level 2 prod-  
 96 ucts require large computational resources, that preclude full dataset re-processing to  
 97 help fully understand trends. A main characteristic of traditional L2 retrievals is the re-  
 98 quirement for a good *a-priori* state for each inversion, making errors in the *a-priori* dif-  
 99 ficult to distinguish from true variability in the data, especially with regard to trends.

100 The stability and accuracy of the AIRS instrument is documented in recent work  
 101 on analyzing 16 years of AIRS radiance anomalies over cloud-free ocean Strow and DeSouza-  
 102 Machado (2020). Geophysical retrievals on the anomalies yielded CO<sub>2</sub>, CH<sub>4</sub>, N<sub>2</sub>O and  
 103 surface temperature time series that compared well against in-situ data from NOAA Global  
 104 Monitoring Laboratories (GML) trace gas measurements and NOAA Goddard Institute  
 105 of Space Studies (GISS) surface temperature data respectively. A significant difference  
 106 between this paper and Strow and DeSouza-Machado (2020) is the nominally clear scenes  
 107 used in this paper are selected uniformly from all over the Earth, while the clear scenes  
 108 in the latter were zonal averages which were sometimes concentrated in certain regions.

109 In this paper we expand upon our initial zonal clear sky analysis, to derive geophys-  
 110 ical trends from 20 years (September 2002 - August 2022) of AIRS measurements over  
 111  $\sim 3 \times 5$  degree tiles covering the Earth, chosen such that the number of observations  
 112 in each tile is roughly equal. An important concept introduced is spectral closure, whereby  
 113 the observed clear sky spectral radiance trends are compared to spectral trends produced  
 114 by running the monthly reanalysis or official NASA retrieved AIRS L3 products through  
 115 an accurate clear sky radiative transfer code; close agreement in different sounding re-  
 116 gions (such as 640-800 cm<sup>-1</sup> for temperature and CO<sub>2</sub>, 1350-1640 cm<sup>-1</sup> for water va-

117 por, 1000-1150  $\text{cm}^{-1}$  for  $\text{O}_3$ ) between the computed and actual observed spectral trends  
 118 imply that trends from those geophysical parameters used in the computations are re-  
 119 alistic while disagreement suggests otherwise. A companion paper will utilize the geo-  
 120 physical trend results to derive Outgoing Longwave Radiation (OLR) trends and non-  
 121 local clearsky feedback parameters. Nominally clear scenes for each tile are picked out  
 122 using a quantile approach; from the time series, radiances trends are made over the en-  
 123 tire Earth, from which geophysical trends are retrieved.

124 Observed infrared spectral trends from AIRS has already been a focus of earlier  
 125 work by Huang et al. (2023) who studied a slightly shorter time period (2002-2020) while  
 126 Raghuraman et al. (2023) converted the radiances to Outgoing Longwave radiation (OLR),  
 127 but neither study involve retrievals from spectral trends to geophysical trends. Instead  
 128 they convert various model trends (such as ERA5) to spectral trends and compare against  
 129 the observed spectral trends. Our earlier work shows we can accurately account for the  
 130 effects of GHG forcings (Strow et al., 2021). In this paper we remove these GHG forc-  
 131 ings from the observed AIRS spectral trends to concentrate on atmospheric temperature  
 132 and water vapor and surface temperature, while the papers by Huang et al. (2023); Raghu-  
 133 raman et al. (2023) include the GHG forcings in the model generated spectral trends.  
 134 Another noteworthy examination of the time evolution of high spectral resolution infrared  
 135 radiances (converted to spectral outgoing longwave radiation (OLR) fluxes) by (Whitburn  
 136 et al., 2021) covered 10 years (2007-2017) of IASI observations. They confirmed that the  
 137 IASI-derived fluxes agreed well with increases in GHG gas concentrations and El-Nino  
 138 Southern Oscillation (ENSO) events within that time frame. A more recent paper Roemer  
 139 et al. (2023) used the 10 year IASI data to derive allsky longwave feedback spectral com-  
 140 ponents (water vapor,  $\text{CO}_2$ , window, ozone) and total values, while also estimating clear  
 141 sky feedback values.

142 We will refer to our results as the AIRS Radiance Trends (AIRS\_RT). Compar-  
 143 isons are made against monthly output from the European Center for Medium Weather  
 144 Forecast fifth generation reanalysis (ERA5) Hersbach et al. (2020) and NASA’s second  
 145 generation Modern-Era Retrospective analysis for Research and Applications (MERRA2)  
 146 Gelaro and Coauthors (2017), and also against the official monthly AIRS L3 products  
 147 which are AIRS v7 L3 Susskind et al. (2014); Tian et al. (2020) and CLIMCAPS v2 L3  
 148 Smith and Barnett (2019, 2020). Detailed geophysical trends and spectral closure stud-  
 149 ies are presented for the ascending (daytime (D)), descending (nighttime (N)) and D/N  
 150 averages.

## 151 2 Datasets used in this study

152 Three main types of datasets are used in this study. The first is the AIRS L1C ra-  
 153 diance dataset we analyzed for this paper, which has both daytime (D) and nighttime (N)  
 154 (ascending and descending) views of the planet. Second is the monthly operational L3  
 155 retrieval data, which are the AIRS v7 and the CLIMCAPS v2 products, also separated  
 156 into D/N data. Finally we also compared to trends from ERA5 and MERRA2 monthly  
 157 reanalysis model fields. The ERA5 monthly dataset is available in 8 averaged time steps,  
 158 so we match to the average AIRS overpass times and compute (D/N) data over the 20  
 159 years, while MERRA2 monthly model fields are only available as one time step; included  
 160 here for completeness we mention the NASA GISS surface temperature dataset, which  
 161 like MERRA2 is only available as a monthly mean. This means four of the datasets : AIRS\_RT  
 162 (from AIRS L1C), AIRS L3 and CLIMCAPS L3, and ERA5 are separable into D/N, while  
 163 the other two (MERRA2 and GISS) are only available as a diurnal averaged value. We  
 164 describe these datasets in more detail below.

## 2.1 The AIRS instrument and L1C dataset

The Atmospheric Infrared Sounder (AIRS) on board NASA’s polar orbiting EOS/Aqua platform has 2378 channels, covering the Thermal Infrared (TIR) spectral range (roughly 649-1613  $\text{cm}^{-1}$ ) and shortwave infrared (2181-2665  $\text{cm}^{-1}$ ). The full widths at half maximum satisfy  $\nu/\delta\nu \sim 1200$ . The (spectral dependent) noise is typically  $\leq 0.2\text{K}$ . The original L1b radiance dataset suffers from spectral gaps and noise contaminated data as detectors slowly fail. These limitations are addressed using a 2645 L1c channel dataset, where spectral gaps and some of the noise “pops” are filled in using principal component reconstruction Manning et al. (2020) and is the dataset used to subset radiances analyzed in this paper. However we note that the results described in this paper used only the actual observed radiances in pristine, stable channels described in Strow et al. (2021) and none of the synthetic channels. The Aqua platform is a polar orbiting satellite with 1.30 am descending (night time over equator) and 1.30 pm ascending (daytime over equator) tracks. Each orbit takes about 90 minutes, with the 16 passes yielding almost twice daily coverage of the entire planet. About  $\sim 3$  million AIRS spectral observations have been obtained daily since AIRS became operational in late August 2002. The instrument has provided data almost continuously since then though there have been some shutdowns (each spanning a few days) such as during solar flare events.

In this paper we use the re-calibrated 2645 channel L1C radiance data Strow and DeSouza-Machado (2020) instead of the 2378 L1B data. 20 years (spanning September 1, 2002-August 31, 2022) of AIRS L1C radiance data is gridded into 4608 tiles covering the Earth : 72 longitude boxes which are all  $5^\circ$  in width, and 64 latitude boxes which are approximately  $2.5^\circ$  in width at the tropics but wider at the poles to keep the number of observations per 16 day intervals (which is the repeat cycle of the AIRS orbit on the Aqua satellite) roughly the same. This way there are  $\sim 12000$  observations per 16 days per tile, which are roughly equally divided between the ascending/daytime (D) and descending/nighttime (N) tracks. In this paper we discuss results for both the ascending and descending tracks using a retrieval based on the longwave (LW) and midwave (MW) regions of the spectrum (640-1620  $\text{cm}^{-1}$  or 6-15  $\mu\text{m}$ ).

In this paper our trend retrievals use only the AIRS channels are stable in time, as quantified in Strow et al. (2021). For example the shortwave (SW) channels are drifting at a higher rate than the LW/MW channels, which can lead to incorrect surface temperature rates, and are avoided in this paper. Similarly there are many channels in the LW and MW whose detectors are drifting in time, and which are also not used here. For example there are some higher wavenumber (shorter wavelength) channels past the ozone band which have a significant drift in time, possibly due to changes in the polarization of the scan mirror coating with time. Therefore compared to other AIRS operational products used in this paper, our results use channels that are demonstrated to have high stability Strow et al. (2021). We do note that some of the observed drifts in the AIRS channels stabilized after 6 years, so their impact is reduced when looking at 20 year trends.

## 2.2 Reanalysis Model fields

The ERA5 fifth generation reanalysis product from the European Center for Medium Range Weather Forecasts is freely available on monthly timescales from the Copernicus Climate Data Store. This monthly dataset is output at 37 pressure levels at  $0.25^\circ$  horizontal resolution Hersbach et al. (2020), which is further subdivided into eight 3-hour averages per month (corresponding to 00,03,06,...21 UTC). For each month from September 2002-August 2022 we downloaded the surface temperature and pressure fields, as well as atmospheric temperature, water vapor and ozone fields. These are then collocated to each tile center using 2D spatial interpolation, as well as time interpolated according to the average AIRS overpass time as a function of month. From the resulting monthly time-

216 series of reanalysis model fields for each tile, we generated (a) thermodynamic trends for  
 217 surface temperature, air temperature, water vapor and ozone model fields (b) a 20 year  
 218 average thermodynamic profile in order to produce jacobians for the linear trend retrievals  
 219 (c) by using the model fields as input to the clear sky SARTA radiative transfer code Strow,  
 220 Hannon, DeSouza-Machado, et al. (2003) a monthly time series of clear sky radiances  
 221 for each tile was generated, from which we could compute radiance trends. We did this  
 222 for both the ascending and descending datasets.

223 The MERRA version 2 (MERRA2) re-analysis used in this paper is the second gen-  
 224 eration Gelaro and Coauthors (2017) product from NASA’s Global Modeling and As-  
 225 simulation Office. The monthly data we use is available on 42 pressure levels at a hor-  
 226 izontal resolution of  $0.5^\circ \times 0.625^\circ$ , but only one monthly mean diurnally averaged out-  
 227 put is available per month. Similar to the ERA5 output, we colocated the MERRA2 sur-  
 228 face temperature, atmospheric temperature, water vapor and ozone fields to our tile cen-  
 229 ters for each month starting September 2002 in order to produce a time series of radi-  
 230 ance and model output, from which radiance and thermodynamic trends could be com-  
 231 puted for comparisons against other datasets in this study; similar to above we also gen-  
 232 erated a monthly time series of clear sky radiances for each tile, from which we could com-  
 233 pute clear sky radiance trends based on MERRA2.

234 The NASA Goddard Institute of Space Studies (GISS) surface temperature data  
 235 v4 surface temperature data 2023 (2005); Lenssen et al. (2019) is a monthly dataset based  
 236 primarily on near surface temperatures land stations, and data from ships and buoys.  
 237 As with MERRA2 we obtained one monthly mean dataset per month, which we could  
 238 not separate into descending (N) or ascending (D) tracks.

### 239 **2.3 AIRS L3 Products**

240 NASA routinely produces two retrievals from the AIRS L1C data observed each  
 241 day, which are AIRS v7 Susskind et al. (2014); Tian et al. (2020) and CLIMCAPS v2  
 242 Smith and Barnett (2019, 2020). Both use the cloud clearing process but there are sig-  
 243 nificant algorithmic differences; in particular the AIRS v7 product is initialized by a neu-  
 244 ral net, while CLIMCAPS uses MERRA2 for its initialization. The L2 products are then  
 245 individually turned into L3 monthly products, for both the ascending (daytime) and de-  
 246 scending (nighttime) data. The timeseries of thermodynamic profiles were used as in-  
 247 put to the clear sky SARTA RTA to generate radiances, after which radiance trends and  
 248 thermodynamic trends are also produced.

### 249 **2.4 Other L3 Products**

250 The Microwave Limb Sounder (MLS) monthly binned water vapor (H<sub>2</sub>O) mixing  
 251 ratio dataset Lambert et al. (2021), which contains data at spatial coverage  $\pm 82^\circ$  lat-  
 252 itude, at a spatial resolution of  $4^\circ \times 5^\circ$  and useful vertical range between 316 and 0.00215  
 253 hPa was used in this paper to improve retrieval trends in the upper atmosphere.

## 254 **3 Filtering the Observational Data for clear scenes**

255 Here we discuss the “clear scene” selection from all the observed data stored for each  
 256 of the  $72 \times 64$  tiles. Ideally we would prefer to use a MODIS cloud fraction product (1  
 257 km) colocated to the 15 km AIRS footprints, but this is presently unavailable. Our ear-  
 258 lier work used an uniform clear flag over ocean Strow et al. (2021) which will not work  
 259 well over land because of surface inhomogeneity. In this section we discuss an alterna-  
 260 tive clear filter based on the hottest 10 percent of AIRS observations that are present  
 261 inside any 16 day tile, over any location.

262

### 3.1 Observed BT1231 Distributions

263

264

265

266

267

268

269

270

271

272

273

274

275

276

277

278

279

280

281

The radiances measured in thermal infrared window region (800-1000  $\text{cm}^{-1}$  and 1100-1250  $\text{cm}^{-1}$ ) are dominated by the effects of the surface temperature, water vapor continuum absorption and cloud/aerosol effects. The effects of water vapor continuum absorption is largest in hot and humid tropical scenes (depressing the observations relative to surface temperatures by about 5-6 K, which reduces to about 2 K at  $\pm 50^\circ$ ) and is almost negligible for cold, dry scenes (less than 1 K). Scattering and absorption by liquid and ice clouds also affects the window region (Deep Convective Clouds can depress the window channel observations by as much as 100 K relative to surface temperatures). For each tile, we use the 1231.3  $\text{cm}^{-1}$  observation as our representative window channel (AIRS L1C channel ID = 1520), as it is minimally impacted by weak water vapor lines. Changed to Brightness temperature (BT) the observation in this 1231.3  $\text{cm}^{-1}$  channel (BT1231) therefore serves as a measure for the cloudiness of an observation : if there are no or low or optically thin clouds, it will effectively measure the surface temperature, but as the clouds get thicker and higher, it will measure the cold cloud top temperatures. For any tile during any 16 day observation periods, we can compute quantiles  $Q$  based on the observed BT1231 to screen between cloudy and partially clear scenes. We chose different BT1231 quantiles (so quantile  $Q_{0.XY}$  will have a numerical value  $BT_{1231_{Q_{0.XY}}}$  associated with it) and show below the data contained between  $Q_{0.90}$  and  $Q_{1.00}$  can be considered “almost free of clouds.”

282

283

284

285

286

287

288

289

290

291

292

293

294

Figure 1 shows all the BT1231 observations for a chosen 16 day timestep in the form of a zonally averaged histogram (normalized probability distribution functions (PDFs)), with latitude on the vertical axis and BT1231 on the horizontal axis. The colorbar is the PDF value, and we used data spanning August 27, 2012 - September 11, 2012 which is approximately half way through the 20 year AIRS mission dataset used in this paper. The curves show the zonally averaged BT1231 values of the minimum ( $Q_{0.00}$ ) in dark cyan, mean (thick red), median ( $Q_{0.50}$  in orange), maximum ( $Q_{1.00}$  in light cyan); also shown are a handful of other zonally averaged BT1231 values, for example  $Q_{0.80}$ ,  $Q_{0.90}$  (thick black curve),  $Q_{0.95}$  and  $Q_{0.97}$ . The distributions are skewed to the left (negative skewness), as confirmed by the mean being less than the median. We also point out that even  $Q_{0.80}$  sees much of the surface from the southern tropics to the northern polar region. The 220 K horizontal axis cutoff means we do not see the very cold (190 K) observations over the winter Antarctic.

295

296

297

298

299

300

301

302

303

304

305

306

307

308

The figure shows the expected qualitative features, for example (1) the tropical PDFs peak at around 295 K, but show some warmer observations, as well much colder observations (below 230 K) corresponding to Deep Convective Clouds (DCC); this gives a dynamic range of almost 100 K at the tropics (2) the BT1231 observed over the Southern Polar (polar winter) regions are much colder than the BT1231 observed over the Northern Polar (polar summer) regions and (3) the reddish peaks in the  $30^\circ\text{N}$  -  $40^\circ\text{N}$  are a combination of the marine boundary layer (MBL) clouds and warmer summer land temperatures. Figure 1 shows on average the cloud effect at the tropics is an additional modest 20 K (difference between  $Q_{0.90}$  and  $Q_{0.50}$ ) compared to the 100 K dynamic range. This is because the cloud fractions and cloud decks in the individual observations have effectively more clouds (with larger cloud fraction in the FOV) lower in the atmosphere than higher up; the net effect is that in the window region the atmosphere is on average radiating from the lower (warmer) altitudes, and so spectra whose BT1231 values are larger than  $BT_{1231_{Q_{0.80}}}$ , see much of the surface emission as well.

309

310

311

312

We now use the above plots to select “almost clear” scenes. For any one tile, we define set  $\Psi_{0.XY}$  to have all observations  $i$  whose BT1231 lies between quantiles  $Q_{0.XY}$  and  $Q_{1.00}$ ,  $\{i \mid BT_{1231_{Q_{0.XY}}} \leq BT_{1231}(i) \leq BT_{1231_{Q_{1.00}}}\}$ . In what follows  $Q_{0.XY}$

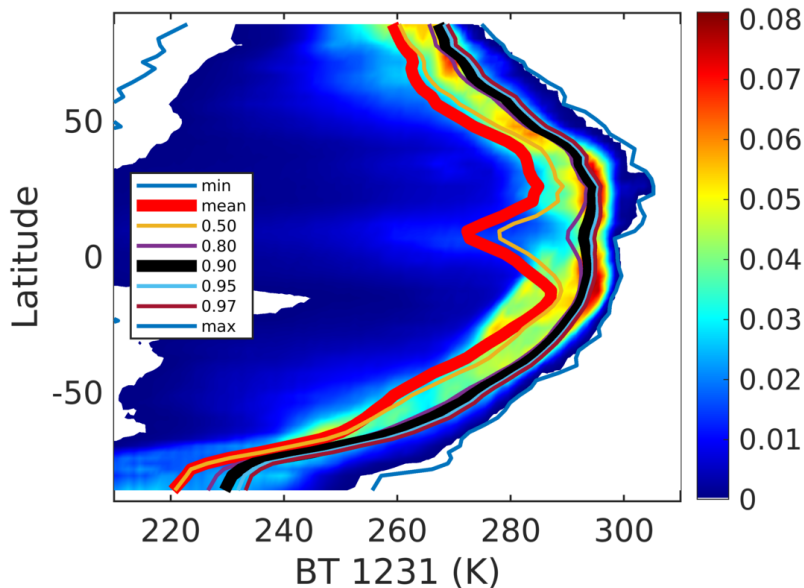


**Figure 1.** Zonally averaged BT1231 normalized histograms (probability distribution functions) as a function of latitude and temperature bin, for an 2012/08/27 - 2012/09/11 timespan (colorbar) and quantiles (curves). The thick black curve is the  $Q_{0.90}$  quantile (and above) used in this paper, and is very close to the maximum  $Q_{1.00}$  quantile.

313 is the radiances averaged over all the observations  $i$  which are in the set  $\Psi_{0.XY}$ , namely

$$r_{Q_{0.XY}}(\nu) = \frac{1}{N_{0.XY}} \sum_{i \in \Psi_{0.XY}} r_i(\nu) \quad (1)$$

314 where  $r_i(\nu)$  are the  $N_{0.XY}$  individual observations in set  $\Psi_{0.XY}$ . In this section we only  
 315 use the  $\nu = 1231 \text{ cm}^{-1}$  channel, but in later sections we easily form averages for all 2645  
 316 channels, at any 16 day time step for any tile.

317 We tested different quantile sets  $\Psi_{0.XY}$  to see which one can reliably be considered  
 318 to provide a nominally “cloud free” global dataset, and chose the  $Q_{0.90}$  average (ie de-  
 319 fined as averaged over the  $\Psi_{0.90}$  set) as the one to use for the rest of this paper, unless  
 320 explicitly stated otherwise. The tests primarily involved comparisons to scenes produced  
 321 by the uniform/clear sky filter described in Strow and DeSouza-Machado (2020) for the  
 322 same August 27, 2012 - September 11, 2012 sixteen day timespan. This latter filter se-  
 323 lects clear scenes by both testing for uniformity (to within 0.5 K) across a  $3 \times 3$  group-  
 324 ing of AIRS scenes and also using a criteria that the observed window channel observa-  
 325 tions should be within  $\pm 4$  K of clear-sky simulations using thermodynamic parameters  
 326 supplied by reanalysis models. The results are shown in the left hand plot of Figure 2,  
 327 plotted on a  $1^\circ \times 1^\circ$  grid. We note in this plot the uniform/clear scenes that are plotted  
 328 are limited to those over ocean, and for solar zenith less than  $90^\circ$  (daytime), which au-  
 329 tomatically filtered out many of the views over the (wintertime) Southern Polar region.  
 330 Immediately apparent are the gaps produced by the uniform/clear filter *e.g.* in the Trop-  
 331 ical West Pacific or off the western coasts of continents where there are clouds. The gaps  
 332 can be changed by *e.g.* changing the 4K threshold to allow more or fewer scenes through  
 333 the filter.

334 The center plot shows for all tiles, the daytime scenes selected for the  $Q_{0.90}$  av-  
 335 erage for the same time period, on the same  $1^\circ \times 1^\circ$  grid. Compared to the left hand plot,



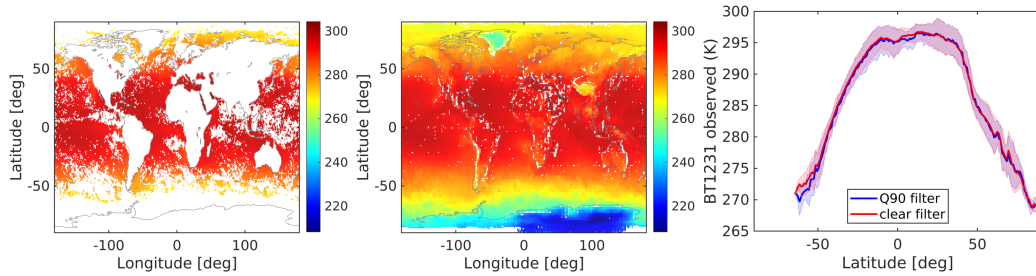


**Figure 2.** Clear scenes for the same 2012/08/27 - 2012/09/11 timespan selected by (left) an uniform/clear sky filter and (center) the Q0.90 average described in this paper. The right hand plot shows the mean (over ocean) observed BT1231 as a function of latitude, for the two selections; the difference is about  $0\text{ K} \pm 1\text{ K}$  in most region except in the southern midlatitudes where the Q0.90 average produced scenes that were about 1 K cooler on average.

336 the spatial coverage is almost complete, as the Q0.90 average always has the hottest 10%  
 337 of the observations. At this  $1^\circ$  resolution, used for comparison with the uniform/clear grid  
 338 filter described in the previous paragraph, gaps are seen in regions where for example  
 339 the local topography means observations over mountains would be colder than the sur-  
 340 rounding coastal or plain regions. This is not a concern since zooming back out to the  
 341 coarser  $3^\circ \times 5^\circ$  tile resolution, will include Q0.90 data for the quantile and trending anal-  
 342 ysis.

343 To compare the mean observations we remove the over-land and over-polar region  
 344 data from the center plot. The right hand plot shows the mean observed BT1231 from  
 345 the  $1^\circ \times 1^\circ$  grid from the uniform/clear sky filter as a function of latitude, compared to  
 346 the  $1^\circ \times 1^\circ$  grid from the Q0.90 scenes. The difference between the uniform/clear versus  
 347 Q0.90 average is within about  $0.25\text{ K} \pm 1\text{ K}$  across the southern tropics to the north-  
 348 ern midlatitudes, though the bias rises to about 1 K by about  $-50^\circ\text{S}$ . We consider this  
 349 an acceptable difference, as we could tune the thresholds for the uniform/clear filter to  
 350 *e.g.* change the areal coverage and/or number of clear scenes and hence comparisons to  
 351 the Q0.90 scenes.

352

353 The results presented in this section have been checked for robustness, using other  
 354 16 day intervals spanning the four seasons. We conclude that for any 16 day timestep  
 355 the radiances used in the Q0.90 average (a) produces almost complete spatial coverage  
 356 of the Earth, (b) selects scenes whose average BT1231 is very close to the average BT1231  
 357 from scenes selected using an uniform/clear filter (c) trends from that quantile typically  
 358 differ by less than  $\pm 0.002\text{ K yr}^{-1}$  from the other quantiles and (d) this selection pro-  
 359 duces spectral trends which compare well against those obtained from the quality assured  
 360 binned AIRS CCR data record Manning (2022). Together these imply the Q0.90 aver-  
 361 age is an acceptable proxy for “clear scenes”. For the remainder of the paper we there-  
 362 fore consider Q0.90 as consisting of nominally clear observations whose BT1231 lies be-  
 363 tween the 90th quantile and hottest observation. Our retrievals using this  $Q_{0.90} \rightarrow Q_{1.00}$   
 364 averaged dataset (shortened to Q0.90) is referred to as AIRS\_RT in what follows.

### 365 3.2 Observed trends from the Q0.90 Quantiles

366 Having selected the Q0.90 observations, for each tile the average radiance per 16  
 367 day interval is computed. With two sixteen day periods not available (Aqua platform

368 or AIRS shutdowns during *e.g.* solar flare events) this gives a total of 457 time steps over  
 369 20 years. Anomalies are formed from this time series, and then de-seasonalized to give  
 370 the spectral radiance trends and error estimates Strow and DeSouza-Machado (2020) us-  
 371 ing Matlab *robustfit*:

$$r_{\text{observations}}^{16 \text{ days}}(t) \sim r_{\text{fit}}(t) = r_o + a_1 t + \sum_{i=1}^4 c_i \sin(n2\pi t + \phi_i) \quad (2)$$

372 with  $a_1$  and its associated uncertainty, both converted to brightness temperature (BT),  
 373 being the trends in  $\text{K yr}^{-1}$ . Using sub-harmonics in the fit did not produce any notice-  
 374 able change in the AIRS\_RT retrievals (described below).

375 The left panel of Figure 3 shows the descending orbit (nighttime) 20 year (Septem-  
 376 ber 2002- August 2022) global averaged spectral observations for the five quantiles men-  
 377 tioned above. We note the spectra in most of the plots in this section are weighted by  
 378 the *cosine(latitude)* of the tiles, unless otherwise stated. In addition we only show the  
 379  $640\text{-}1640 \text{ cm}^{-1}$  region, and ignore the shortwave  $2050\text{-}2750 \text{ cm}^{-1}$  region since the AIRS  
 380 SW channels are drifting relative to the LW Strow and DeSouza-Machado (2020). Spec-  
 381 tral averages constructed from Figure 1 would have this same behavior, namely that in  
 382 the window region the mean spectrum of data populating the warmer quantiles (Q0.80,  
 383 Q0.90, Q0.95, Q0.97) as defined in Equation 1 are on the order of a Kelvin apart, and  
 384 have about half/quarter that difference in the optically thicker regions dominated by  $\text{H}_2\text{O}$   
 385 and/or  $\text{CO}_2$  absorption respectively.

386 The right hand panel of Figure 3 shows (top) the trends and (bottom) the  $2\sigma$  trend  
 387 uncertainties for these quantiles, in  $\text{K yr}^{-1}$ . We emphasize that the top right panel shows  
 388 that the spectral trends for the quantiles lie almost on top of each other; the difference  
 389 between the Q0.50 and other trends is at most about  $+0.003 \text{ K yr}^{-1}$  (out of a  $0.02 \text{ K}$   
 390  $\text{yr}^{-1}$  signal) in the window region (and about  $+0.0045 \text{ K yr}^{-1}$  in the troposphere tem-  
 391 perature sounding channels), or less than 10%. Similarly the largest trend uncertainty  
 392 in the bottom panel is for Q0.50. This implies that clouds effects in the infrared do pro-  
 393 duce the largest variability (blue curve) but on average for the infrared are not chang-  
 394 ing much, so the  $+0.022 \text{ K yr}^{-1}$  window region trends are dominated by surface tem-  
 395 peratures changes and to a lesser extent by water vapor changes.

396 TOA radiances in the  $15 \text{ um}$  ( $700\text{-}800 \text{ cm}^{-1}$ ) region are impacted by two effects  
 397 (a) the increased optical depths due to increasing atmospheric  $\text{CO}_2$  leads to atmospheric  
 398 emission from higher altitudes/lower temperatures, resulting in almost a  $-0.06 \text{ K/year}$   
 399 signal for the troposphere, and (b) the atmospheric temperature increases (again about  
 400  $+0.02 \text{ K yr}^{-1}$ ). Also of interest is the trends in the stratosphere ( $650\text{-}700 \text{ cm}^{-1}$ ) changes  
 401 which consists of a stratospheric cooling signal (negative) and emission higher up due  
 402 to increased  $\text{CO}_2$ ; combining to give a net zero effect over 20 years, also seen in Raghuraman  
 403 et al. (2023). The  $\text{H}_2\text{O}$  signal is evident in the  $1400\text{-}1625 \text{ cm}^{-1}$  region, and is negative;  
 404 in other words, increasing temperatures have led to increased atmospheric amounts of  
 405  $\text{H}_2\text{O}$ , and the water vapor feedback has reduced the amount of outgoing flux in that re-  
 406 gion. By extension, this also happens in the Far Infrared regions affected by water va-  
 407 por; current sounders do not make direct measurement in the  $10\text{-}600 \text{ cm}^{-1}$  region so at  
 408 present this can only be inferred; however in the near future it is anticipated the Far In-  
 409 frared Outgoing Radiation Understanding and Monitoring (FORUM) mission Palchetti  
 410 et al. (2020) will provide data to fill in this important gap in the future.

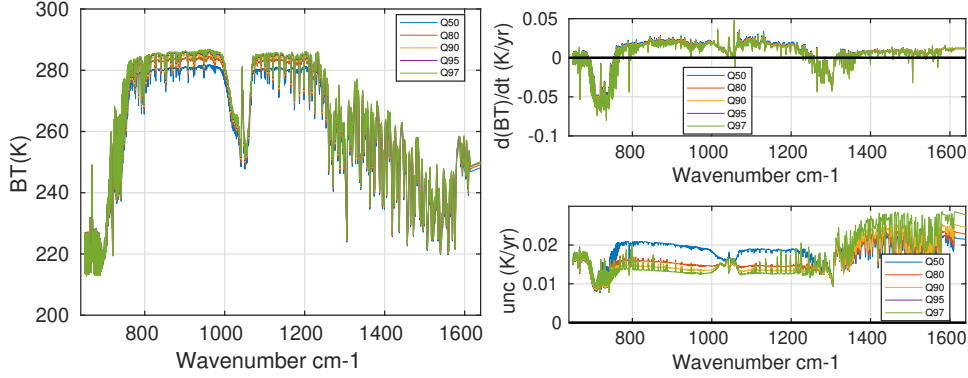


**Figure 3.** 20 year trends from different observation quantiles. The left hand panel shows the mean globally averaged BT observations from 20 years of AIRS data, for quantiles Q0.50,0.80,0.90,0.95,0.97 as described in the text. The right hand panel shows (top) the globally averaged trends for those different quantiles and (bottom) the spectral uncertainty in the trends. The nighttime (descending) trends are shown in these plots.

#### 4 Spectral closure : comparisons between observed and simulated spectral trends

Previous work Strow and DeSouza-Machado (2020) has demonstrated that the radiances from AIRS are climate quality, if one restricts the channel set to the  $\sim 450$  channel set that is largely immune to nonphysical drifts Strow et al. (2021). In this section we describe a way to test the quality of the monthly thermodynamic output from reanalysis and/or L3 products which are all in geophysical space, against the AIRS L1C observational data which is in radiance space. This is accomplished by geolocating the monthly (ERA5) surface temperature, air temperature, water vapor and ozone fields to tile centers as described in Section 2.2, which are then input and run through the SARTA fast model Strow, Hannon, DeSouza-Machado, et al. (2003), for the entire 20 years. Spectral radiance trends were then computed from these time series of (clear sky) spectral radiances. The conversion of L3 retrieval and NWP reanalysis trends to a radiance time series, provides a rigorous check of their accuracy against the observed AIRS L1C radiance trends which are validated to be highly accurate.

The simulations included realistic column linearly-increasing-with time mixing ratios for  $\text{CO}_2$ ,  $\text{CH}_4$  and  $\text{N}_2\text{O}$  for the ERA5 spectra, as well as land or ocean surface emissivity co-located to tile centers together with view angles of about  $22^\circ$ . From these the ERA5 spectral trends were derived similarly to what was described above for the AIRS observation spectral trends.

Figure 4 shows the descending (night) zonally averaged results in  $\text{K yr}^{-1}$ , allowing us to compare the Q0.90 nominally clear AIRS observed spectral trends, to those simulated using monthly ERA5 fields (without clouds). The center panel shows the spectral trend uncertainties from the observations, also in  $\text{K yr}^{-1}$ . In the next section we derive geophysical trends from these (AIRS observed) spectral trends, and the similarities/differences in geophysical trends can be partially understood from the similarities/differences in the spectral trends. For example, the  $\text{H}_2\text{O}$  sounding region ( $1350\text{-}1600 \text{ cm}^{-1}$ ) shows roughly similar (positive) trends in the tropics and mid-latitudes; there are some slight differences in the high altitude channels ( $1450\text{-}1550 \text{ cm}^{-1}$  region). The following sections

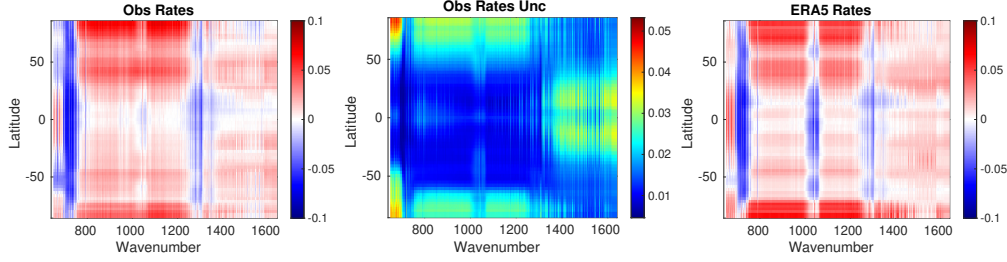


**Figure 4.** 20 year zonally averaged spectral brightness temperature trends (in  $\text{K yr}^{-1}$ ) for (left) AIRS Q0.90 observations and (right) clear sky simulations using ERA5 monthly model fields. The center panel shows the AIRS Q0.90 spectral uncertainties. The ERA5 simulations included linear trends of  $\text{CO}_2$ ,  $\text{CH}_4$  and  $\text{N}_2\text{O}$ , while the  $\text{O}_3$  trends in ERA5 are from the reanalysis itself.

442 shows that there are subtle differences in these trends, which manifest as differences in  
 443 tropospheric water vapor trends. Observations and simulations both have positive  $\text{dB T}/\text{dt}$   
 444 in the  $800\text{-}960, 1150\text{-}1250 \text{ cm}^{-1}$  region, indicating surface warming; however the ERA5  
 445 simulation show more warming in the southern polar regions than do the AIRS obser-  
 446 vations. In particular note the mean warming in the tropics is less than that in the mid-  
 447 latitudes, and the polar regions show the largest overall change in brightness tempera-  
 448 ture in the window region. Large differences are seen in the  $10 \text{ um}$  ( $1000 \text{ cm}^{-1}$ )  $\text{O}_3$  sound-  
 449 ing region, which are not surprising since ozone assimilation is not a primary goal of ECMWF  
 450 assimilation; here we do not address these as we focus on the changes to the moist ther-  
 451 modynamic state. The window region trends computed using the ERA5 model are more  
 452 positive in the Southern Polar region. Conversely the  $640\text{-}700 \text{ cm}^{-1}$  spectral region is  
 453 positive, especially in the tropics; however the observations show a net cooling trend away  
 454 from the tropics, compared to the ERA simulations. This demonstrates the importance  
 455 of the model  $\rightarrow$  spectral trend comparisons, given the accuracy of the AIRS observations.

456 The paper by (Raghuraman et al., 2023) shows similar figures, but in terms of spec-  
 457 tral OLR trends encompassing the  $0\text{-}2000 \text{ cm}^{-1}$  range, while (Huang et al., 2023) shows  
 458 similar plots for a slightly smaller time period (2002-2020) and using nadir L1B radiance  
 459 dataset which has no or minimal frequency corrections compared to the L1C set we use  
 460 in this paper. (Huang et al., 2023; Raghuraman et al., 2023) and our work all show, ei-  
 461 ther in radiance or OLR space, (a) the increased observed radiance in the window chan-  
 462 nels, due to surface temperature increases (b) the  $\simeq -0.06 \text{ K yr}^{-1}$  decrease in BT in the  
 463  $700\text{-}750 \text{ cm}^{-1}$  troposphere sounding region, which is due to the  $\text{CO}_2$  amounts increas-  
 464 ing; we also see differences in the signs of the BT changes in the  $650\text{-}700 \text{ cm}^{-1}$  strato-  
 465 spheric  $\text{CO}_2$  and temperature channels for some latitudes between AIRS\_RT observa-  
 466 tions and ERA5 simulations (c) increases in the  $1350\text{-}1640 \text{ cm}^{-1}$  water vapor sounding  
 467 region seen in Figures 3 and 5, and (d) the  $1280\text{-}1340 \text{ cm}^{-1}$  decreases are due to  $\text{CH}_4$   
 468 increases.

#### 469 4.1 Sample spectral closure comparisons using other monthly products

470 Here we follow the earlier work of Huang et al. (2023) and convert the ERA5 monthly  
 471 model fields to spectral radiances, after which we compute spectral trends for compar-  
 472 ison to AIRS observations. Spectral closure calculations for the entire 20 year timeseries  
 473 were also generated for the monthly MERRA2 model fields, as well as the monthly AIRS  
 474 v7 L3 and CLIMCAPS L3 retrieved data products. Again only the monthly thermody-  
 475 namics and surface temperature fields for all  $72 \times 64$  tiles were used in these SARTA runs,

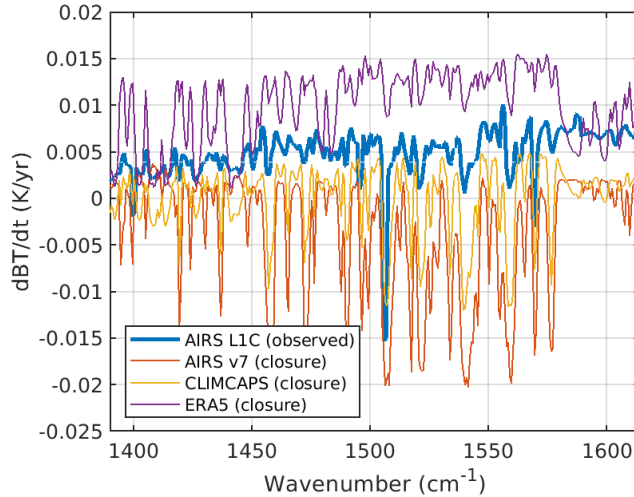


**Figure 5.** Globally averaged spectral trends in the water vapor sounding region : AIRS L1C observations (blue) compared to spectral closure from the standard monthly AIRS L3 retrievals (red) and CLIMCAPS L3 (yellow) and from monthly ERA5 simulations (purple). The reconstructed AIRS\_RT trends very closely match the AIRS L1C observations and are not shown here.

476 with GHG changes added in for each timestep as described above. Spectral trends were  
 477 then computed using Equation 2.

478 We chose just one limited example here to illustrate the power of this approach for  
 479 diagnosing which dataset is more accurate, given that the AIRS spectral trend accuracy  
 480 is already established. Water vapor is highly variable in space and time, meaning wa-  
 481 ter vapor retrievals using hyperspectral sounders radiances differ most from NWP fore-  
 482 casts, in particular because of the typical  $\pm 90$  minute difference between observation  
 483 and forecast, and is where these sounders typically provide the most information. Fig-  
 484 ure 5 show the globally averaged brightness temperature trends (in  $\text{K yr}^{-1}$ ) in the  $1350$   
 485  $- 1650 \text{ cm}^{-1}$  water vapor sounding region. The blue curve shows the trends from the AIRS  
 486 observations used in this paper, while spectral trends constructed from the AIRS L3/  
 487 CLIMCAPS L3 retrievals are in red/yellow and the ERA5 model fields are in purple. The  
 488 AIRS observations and ERA5 constructed spectral trends are positive in this region, while  
 489 the AIRS L3 and CLIMCAPS L3 trends are obviously different, being negative in this  
 490 water vapor sounding region. The subtle differences in these spectral trends arise from  
 491 differences in the geophysical trends between observations and the models themselves,  
 492 and will be addressed in the following sections, where the retrieved and model surface  
 493 temperature, and atmospheric temperature and water vapor geophysical trends will be  
 494 compared and discussed.

495

## 496 **5 Testing the variability of representative points from NWP reanal-** 497 **ysis**

498 Each sixteen day  $3^\circ \times 5^\circ$  tile contains  $\sim 12000$  observations, which means for each  
 499 tile about 600 daytime and 600 nighttime observations are averaged to produce the Q0.90  
 500 dataset per timestep. Conversely there are typically only  $\sim 240$  monthly ERA5  $0.25^\circ$  points  
 501 per  $3^\circ \times 5^\circ$  tile; for  $1^\circ$  resolution AIRS L3 and CLIMCAPS L3 there are even fewer (15)

502 points per tile. This low number of points means we chose a simple solution of using the  
 503 grid cell closest to the center of each  $3^\circ \times 5^\circ$  tile for building the NWP and L3 geophys-  
 504 ical time series. This choice is validated below using the following test to see for exam-  
 505 ple how surface temperature trends would be impacted as we changed the representa-  
 506 tive point for the ERA5 model fields.

507 For the descending overpass we built complete sets of approximately 240 ERA5 points  
 508 per tile per month; at  $0.25^\circ$  resolution one of these is almost certainly at the tile center.  
 509 From these monthly sets, we could either directly read the tile center temperature (our  
 510 default), or compute the average surface temperature per tile, or compute the average  
 511 of the hottest 10% surface temperatures per tile. This was done for all 20 years (240 monthly  
 512 timesteps) after which the three timeseries were trended. Over ocean the differences be-  
 513 tween all three datasets was typically  $-0.001 \pm 0.005 \text{ K yr}^{-1}$ , while over land the differ-  
 514 ences were about  $0.001 \pm 0.01 \text{ K yr}^{-1}$ . This is to be compared to mean trends of about  
 515  $0.014 \pm 0.02 \text{ K yr}^{-1}$  over ocean and  $0.025 \pm 0.04 \text{ K yr}^{-1}$  over land : the spread of the  
 516 ocean and land ERA5 surface temperature trends for the three methods, is much smaller  
 517 than the mean trends. Given that there were far fewer re-analysis points in a grid box  
 518 than tiled Q0.90 observations, coupled with the fact that choosing the 10% warmest pro-  
 519 files would provide an even smaller sample, we chose to use the tile center to be the rep-  
 520 resentative point to co-locate the model fields.

## 521 6 Geophysical Trend Retrieval outline

### 522 6.1 Setting up the Retrieval Problem

523 The observed spectral brightness temperature for a tile at any time  $t$  can be mod-  
 524 eled as

$$BT(\nu, t) = f(X(t), \epsilon(\nu, t), \theta(t)) + \text{NeDT}(\nu) \quad (3)$$

525 where the state vector  $X(t)$  has the following five geophysical state parameters : (1) sur-  
 526 face temperature (ST), (2) atmospheric temperature profile  $T(z)$ , (3) water vapor pro-  
 527 file  $\text{WV}(z)$ , (4) ozone profile  $\text{O3}(z)$  (5) greenhouse gas forcings (GHG) due to  $\text{CO}_2$ ,  $\text{CH}_4$   
 528 and  $\text{N}_2\text{O}$  changing as a function of time  $t$  and  $f(X(t), \epsilon, \theta, \nu)$  is the clear sky radiative  
 529 transfer equation for channel center frequency  $\nu$ . The spectral noise  $\text{NeDT}(\nu)$  for a typ-  
 530 ical tropical “clear scene” is about 0.1 K in window region, increasing to about 1 K in  
 531 the  $15 \mu\text{m}$  temperature sounding channels and about 0.2 K in the  $6.7 \mu\text{m}$  water vapor  
 532 sounding region, but the noise will vary as a function of scene temperature. We parametrize  
 533 the GHGs using single numbers (such as ppm(t) for the  $\text{CO}_2$  column), and include the  
 534 AIRS orbit and viewing angle geometry  $\theta$  and the surface emissivity  $\epsilon(\nu)$ , while we omit  
 535 forward model and spectroscopy errors. We ignore cloud scattering as well as the spa-  
 536 tial variation of the state parameters, emissivity and scan angle geometry within a tile.  
 537 Linearizing the above equation about the time averaged profile, the relationship between  
 538 the observed spectral trends and desired thermodynamic trends is given by

$$\frac{d\overline{BT}(\nu)}{dt} = \frac{\partial f}{\partial \overline{X}} \frac{d\overline{X}(t)}{dt} = K(\nu) \frac{d\overline{X}(t)}{dt} + \cancel{K_{\text{emissivity}}(\nu) \frac{d\overline{\epsilon}(t)}{dt}} \xrightarrow{0} K(\nu) \frac{d\overline{X}(t)}{dt} \quad (4)$$

539 where the matrix  $K(\nu)$  is the thermodynamic jacobian (surface temperature, air  
 540 temperature and trace gases) and we ignore any orbit drifts (changes to  $\theta$ ), instrument  
 541 changes (changes to  $\text{NeDT}(\nu)$ ) and surface emissivity ( $\epsilon(\nu)$ ); the last assumption is in-  
 542 vestigated in a later section. The overbars on parameters  $X$  denotes this is a time av-  
 543 erage (linear trend) that we are working with, and we have converted from radiances in  
 544 Equation 2 to brightness temperatures in Equations 3 and 4.

545

## 6.2 Jacobian calculations

546

547

548

549

550

551

552

553

554

555

556

557

558

559

560

561

562

563

For a typical clear sky tropical sky atmosphere, the 800 - 1200  $\text{cm}^{-1}$  window region has surface temperature (SKT) jacobians which are about +0.5 to +0.75 K per degree SKT change and -0.75 to -0.25 K per 10% change in column water vapor. The spectral variability in these window region jacobians is primarily due to reducing water continuum absorption as you move from the 800  $\text{cm}^{-1}$  end to the 1200  $\text{cm}^{-1}$ ; consequently the surface temperature jacobians becomes closer to unity and the column water jacobians become closer to zero as water vapor amount decreases (drier atmospheres in the mid-latitudes and polar regions). The hyperspectral channels used in this work help separate out these two competing changes, which we validate against other datasets in this study. As seen in Figure 4 typical magnitudes of the spectral trends on the left hand side of Equation 4 are less than about 0.1 K per year. Equation 4 is in the usual inversion form  $\delta y = K\delta x$ , and the Optimal Estimation (Rodgers, 2000) solution used to solve the anomaly time series in Strow et al. (2021) is also used here. The noise term used for the trend retrieval  $NeDT(\nu)$  is not the instrument noise since each 16 day point in our time series is averaged over hundreds of observations as earlier described; instead the uncertainty is that due to inter-annual variability in the linear trends obtained from the trend fitting in Equation 2. Examples of typical noise values are shown in the bottom right hand panel of Figures 3.

564

565

566

567

568

569

570

571

572

573

574

575

576

577

578

ERA5 monthly model fields at tile centers, together with time varying concentrations of GHG such as  $\text{CO}_2$ , were averaged over 20 years so jacobians could be computed. The GHG concentrations were a latitude dependent increase of about 2.2  $\text{ppm yr}^{-1}$  for  $\text{CO}_2$  derived from the CarbonTracker Peters et al. (2007) (CarbonTracker CT-NRT.v2023-4, <http://carbontracker.noaa.gov>) model data at 500 mb. Our pseudo-monochromatic line by line code kCARTA De Souza-Machado et al. (2018, 2020) was used with these averaged profiles to produce accurate analytic jacobians. The HITRAN 2020 line parameter database Gordon and Rothman (2022), together with MT-CKD 3.2 and  $\text{CO}_2, \text{CH}_4$  line mixing from the LBLRTM suite of models Clough et al. (2005) were used in the kCARTA optical depth database De Souza-Machado et al. (2018). A 12 month geographical land-varying spectral emissivity database spanning one year from Zhou et al. (2011) was used, while ocean emissivity came from Masuda et al. (1988). The atmospheric temperature, water vapor and ozone profile jacobians, and the surface temperature and column jacobians for the GHG gases such as  $\text{CO}_2$  and  $\text{CH}_4$  and  $\text{N}_2\text{O}$ , were then convolved using the best estimate AIRS Spectral Response Functions Strow, Hannon, Weiler, et al. (2003).

579

580

581

582

583

Tests done for this paper, together with the results in Strow et al. (2021), established that jacobians derived from MERRA2 versus ERA5 produced no significant differences in the context of retrieved trends or anomalies done for this paper, as the uncertainty in linear trends due to inter-annual variability dominates over any uncertainty (or differences between) model fields.

584

585

## 6.3 Optimal Estimation Retrieval : State vector, covariance matrices and *a-priori*

586

587

588

589

590

591

592

593

594

595

Using monthly ERA5 model fields averaged over 20 years, for each of the  $64 \times 72$  tiles we computed analytic jacobians for the following (vector) atmospheric thermodynamic variables [fractional water vapor, fractional ozone and temperature] together with (scalar) surface temperature, where we retrieved fractional gas concentration trends  $d\text{frac}X/dt = 1/X_{avg}(z)dX_{avg}(z)/dt$  to keep all values in the state vector at about the same magnitude. A single iteration Optimal Estimation retrieval Rodgers (2000) is used to simultaneously solve for the geophysical parameter trends. As in (Strow & DeSouza-Machado, 2020) the geophysical covariance uncertainty matrices are a combination of Tikonov and covariance regularization. The uncertainties for the covariance matrices were typically [0.1,0.25,0.45]  $\text{K yr}^{-1}$  for the surface/tropospheric/stratospheric temperature trends, and

596 [0.04/0.02] yr<sup>-1</sup> for the fractional tropospheric/stratospheric water vapor trends. Tikonov  
 597 L1 regularization (Rodgers, 2000) also included, with the scalar factor multiplying this  
 598 regularization corresponding to about 1/10 the covariance uncertainties. The spectral  
 599 uncertainties used in the retrievals come from the above mentioned trend uncertainties.  
 600 For completeness we note that a sequential retrieval (see for example Smith and Bar-  
 601 net (2020)) produces very similar geophysical trends.

602 Here we emphasize four points about our geophysical trend retrievals, which sets  
 603 us apart from trends derived from other datasets. Firstly the *a-priori* trend state vec-  
 604 tor is zero ( $dST/dt = dT(z)/dt = dQ(z)/dt = 0$ ) for all geophysical parameters, except  
 605 for water vapor where we enforced constant (or slightly increasing) relative humidity as  
 606 as described below. This ensures traceability of our retrieval is straightforward especially  
 607 wherever the AIRS instrument has sensitivity. For example the 300 - 800 mb water va-  
 608 por trend retrievals will be based on the data only, thereby insulating us from any possi-  
 609 ble *a-priori* information from *e.g.* climatology or NWP models, unlike the operational  
 610 AIRS V7 or CLIMCAPS retrievals which use first guesses based on neural net and MERRA2  
 611 respectively.

612 Secondly as seen in Figures 4 and 5, in the 15  $\mu m$  region there is a large spectral  
 613 overlap signal (-0.06 K yr<sup>-1</sup>) from the increasing CO<sub>2</sub>, which is much larger than the  
 614 expected atmospheric temperature trend (0.01 K yr<sup>-1</sup>). These correlations makes it dif-  
 615 ficult to jointly retrieve both temperatures changes and changes in well mixed GHGs such  
 616 as CO<sub>2</sub>. We chose to focus on retrieving temperature changes only, by spectrally remov-  
 617 ing the effects of changing CO<sub>2</sub>, CH<sub>4</sub> and N<sub>2</sub>O GHG concentrations. This was done by  
 618 using the GHG trends estimated from NOAA ESRL CarbonTracker data multiplied by  
 619 the appropriate GHG gas column jacobian (CO<sub>2</sub>,N<sub>2</sub>O and CH<sub>4</sub> and CFC11,CFC12) com-  
 620 puted as described above using the averaged over 20 years ERA5 monthly profile for each  
 621 tile.

622 Thirdly instead of using all 100 layers described in the AIRS forward model Strow,  
 623 Hannon, DeSouza-Machado, et al. (2003), we combine pairs of layers for a 50 atmospheric  
 624 layer retrieval, as the AIRS radiances contain far fewer than 100 pieces of information  
 625 (see *e.g.* Maddy and Barnett (2008); De Souza-Machado et al. (2018)).

626 Fourthly, modern hyperspectral infrared sounders have highest sensitivity to tem-  
 627 perature and water vapor in the mid-tropopause; see for example the averaging kernels  
 628 in Irion et al. (2018). Using a zero fractional WV trends *a-priori* at all levels, it was fairly  
 629 straightforward to obtain fractional WV(z) trends close to those from the NWP model  
 630 datasets in the 300-850 mb region. In order to improve our results in the lowest layers,  
 631 we enforced a constant relative humidity approximation, which is a well-known, expected  
 632 behavior under global climate change Soden and Held (2006); Sherwood et al. (2010).  
 633 This was done by ignoring the contribution due to water vapor changes in the observed  
 634 BT1231 trend, and using it as an approximation for air temperature trend over ocean;  
 635 this allows us to compute an estimate of how the water vapor would need to change

$$RH(T) = \frac{e}{e_{sat}(T)} \implies \delta(RH) = \frac{1}{e_{sat}(T)} \delta e - \frac{e}{e_{sat}^2(T)} \delta e_{sat}(T) = \frac{1}{e_{sat}(T)} \delta e - \frac{e}{e_{sat}(T)} \frac{L_v}{R_v} \frac{1}{T^2} \delta T \quad (5)$$

636 where  $e, e_{sat}(T)$  are the vapor pressures and we used  $e_{sat}(T) = e_{s0} e^{\frac{L_v}{R_v} (\frac{1}{T_0} - \frac{1}{T})}$  (where  
 637  $L_v, R_v$  are latent heat of vaporization and gas constant respectively) to go from the ex-  
 638 pression in the center to the expression on the right. If we expect the change in RH to  
 639 be zero then  $\frac{\delta e}{e} = \frac{L_v}{R_v} \frac{\delta T}{T^2}$ , where we can use  $\delta T/\delta t \sim d/dt BT1231$ . to approximate the  
 640 *a-priori* fractional vapor pressure rates (or *a-priori* fractional water vapor rates) between  
 641 surface and 850 mb, smoothly tailing to 0 in the upper atmosphere. Subsection 7.2 has  
 642 a similar discussion on a proposed method to alleviate the lack of sensitivity to upper  
 643 atmosphere water vapor. Our default results in this paper are from using the MLS *a-*  
 644 *priori*, unless otherwise stated.



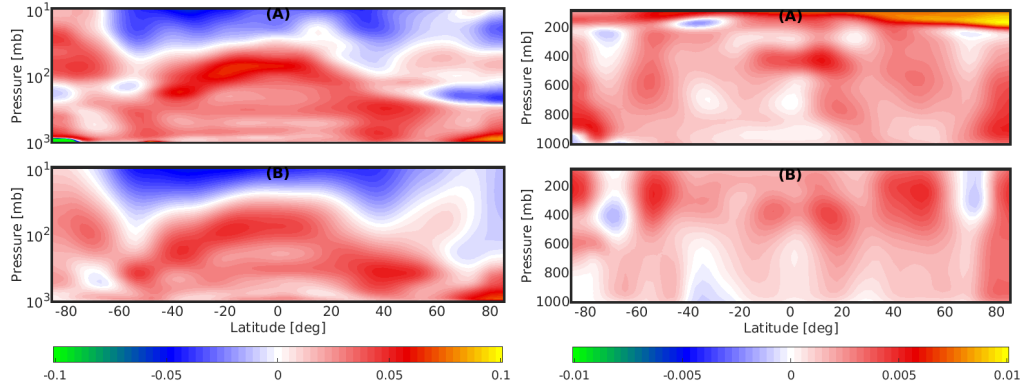


**Figure 6.** Comparing geophysical trends derived directly from ERA5 monthly nighttime fields (top) vs from the OEM retrieval applied to the spectral trends (bottom). Left panel is  $dT/dt$  (in  $K yr^{-1}$ ) while rightmost panel is  $d(\text{fracWV})/dt$  (colorbar in  $yr^{-1}$ ).

#### 645 6.4 Testing on synthetic trend spectra made from ERA5 Reanalysis monthly 646 fields

647 We tested the retrieval code by using it on the simulated nighttime only ERA5 spec-  
648 tral trends, and compared to geophysical trends computed directly from the ERA5 re-  
649 analysis model. Spot checks of the spatial correlations of ERA5 fractional water vapor  
650 and temperature trends versus the trends retrieved from synthetic spectra/our retrieval  
651 algorithm, peaked at 500 mb with correlations of about 0.9, compared to 800 mb cor-  
652 relations of 0.80 and 0.55 for temperature and fractional water vapor trends respectively  
653 and 200 mb correlations of 0.89 and 0.69 for  $dT/dt$ ,  $dWV_{\text{frac}}/dt$ . This is to be expected  
654 since a computation of the water vapor averaging kernels for infrared instruments for ar-  
655bitrary atmospheric profiles typically shows they peak in the 300 mb - 850 mb range and  
656 decrease rapidly away from those regions; conversely the temperature averaging kernels  
657 stay relatively uniform through the free troposphere and above, though they also decrease  
658 close to the surface; see for example Irion et al. (2018); Smith and Barnett (2020); Wu  
659 et al. (2023).

660 Figure 6 shows a sample set of results using nighttime ERA5 model output converted  
661 to spectral trends as described above. The top panels (A) are always the atmospheric  
662 trends computed directly from the monthly ERA5 model fields, while the bottom pan-  
663 els (B) are the atmospheric trends retrieved from the converted ERA5 spectral bright-  
664 ness temperature trends. The left most panel is the atmospheric temperature trend com-  
665 parison (both in  $K yr^{-1}$ ) while the rightmost panel is the fractional atmospheric water  
666 vapor trend comparison (in  $yr^{-1}$ ).

667

668 It is evident from the figure that the tropospheric trends in the tropical and mid-  
669 latitude regions are quite similar, and there are differences in the polar regions and strato-  
670 spheric regions where the AIRS instrument has reduced sensitivity. The atmospheric and  
671 surface trends are shown in Table 1, divided into “all” (which is the entire  $\pm 90$  latitude  
672 range and 0-1000 mb vertical range) and “T/M” which is the tropical/midlatitude region,  
673 which is further reduced to 050-900 mb for air temperature and 300-800 mb for water  
674 vapor. “ERA5 direct” are trends computed directly from the geophysical fields, while “ERA5  
675 spectral” are retrieved from the spectral trends.

	dTz/dt K yr <sup>-1</sup> A SFC-TOA	dTz/dt K yr <sup>-1</sup> T/M 050-900 mb	dSKT/dt K yr <sup>-1</sup> A	dSKT/dt K yr <sup>-1</sup> T/M	dfracWV/dt K yr <sup>-1</sup> A GND-TOA	dfracWV/dt K yr <sup>-1</sup> T/M 300-800 mb
ERA5 direct	0.010 ± 0.038	0.029 ± 0.013	0.020 ± 0.035	0.018 ± 0.032	0.003 ± 0.002	0.002 ± 0.001
ERA5 spectral	0.004 ± 0.033	0.027 ± 0.012	0.019 ± 0.033	0.016 ± 0.029	0.001 ± 0.001	0.002 ± 0.001

**Table 1.** Cosine weighted air temperature, skin temperature, fractional water vapor trends, together with uncertainties. The “ERA5 direct” are directly from the ERA5 geophysical trends, while “ERA5 spectral” are trends retrieved from the converted ERA5 spectral trends.

676

## 6.5 Surface emissivity changes

677

Equation 3 explicitly includes the surface emissivity in the equation of radiative transfer; however Equation 4 assumes this is unchanging. Here we rewrite Equation 4 as

678

679

$$\frac{d\overline{BT(\nu)}}{dt} - K_{emissivity}(\nu) \frac{d\overline{\epsilon(t)}}{dt} \rightarrow \frac{d\overline{BT'(\nu)}}{dt} = K(\nu) \frac{d\overline{X(t)}}{dt} \quad (6)$$

680

681

682

683

684

685

686

687

688

689

690

Ocean emissivity has a dependence on windspeed Masuda et al. (1988). Lin and Oey (2020) and other literature suggest wind speed increases of  $+2.5 \text{ cm s}^{-1} \text{ yr}^{-1}$  have occurred between 1993-2015 in the tropical Pacific, and smaller (or close to zero) values elsewhere. The monthly ERA5  $u10, v10$  10 m speeds for the 20 year time period in this paper also showed the maximum absolute trend was  $0.09 \text{ m/s/year}$  (over the Southern Ocean) while the global ocean mean and standard deviation were  $0.006 \pm 0.022 \text{ m s}^{-1} \text{ yr}^{-1}$ ; The emissivity changes over ocean using a  $0.025 \text{ m s}^{-1}$  wind speed change are on average on the order of  $1 \times 10^{-6}$  per year in the thermal infrared window (or about  $0.0003 \text{ K yr}^{-1}$  change in the window region); assuming the optical properties of water do not substantially change with the  $\sim 0.02 \text{ K}$  increases seen in all the datasets considered in this paper, these very small emissivity changes are of no consequence.

691

692

693

694

695

696

697

698

699

700

701

702

703

704

705

706

707

708

709

710

711

712

Land emissivity changes were estimated as follows. A global monthly mean emissivity database, the Combined ASTER and MODIS Emissivity over Land (CAMEL v003) has recently been released Borbas et al. (2018). We matched the tile centers to the database for the  $20 \times 12$  months spanning our 2002/09 - 2022/08 time period, and computed the emissivity trends over land; the results (not shown here) were on the order of  $-1 \times 10^{-4}$  and  $+3 \times 10^{-4}$  in the  $800\text{-}960 \text{ cm}^{-1}$  and  $1100\text{-}1250 \text{ cm}^{-1}$  regions respectively, averaged over the land observations. For each tile the  $K_{emissivity}(\nu) \frac{d\overline{\epsilon(t)}}{dt}$  term was estimated by running SARTA with the default emissivity, then differencing with the SARTA output obtained when the emissivity trends were added on. Averaged over the planet, the spectral changes arising from these emissivity changes were much smaller than the spectral trends seen in Figure 3, about  $-0.001 \text{ K yr}^{-1}$  between  $800\text{-}960 \text{ cm}^{-1}$  and about  $+0.002 \text{ K yr}^{-1}$  on the  $1100\text{-}1250 \text{ cm}^{-1}$  region (which we do not use in our retrieval, since many of the channels are synthetic and the real channels are drifting (Strow et al., 2021)). The land only results were roughly three times these magnitudes. Using these emissivity jacobians on the left hand side of Equation 6 and running the retrieval on the adjusted spectral trends over land, resulted in about at most  $0.01 \text{ K}$  increases to the zonally averaged surface temperature changes over land; zonally averaged these largest differences were at about  $40^\circ\text{N}$  to  $60^\circ\text{N}$  and  $-25^\circ\text{S}$  to  $+15^\circ\text{N}$ , due to emissivity decreases; the  $20^\circ\text{N}$  to  $+35^\circ\text{N}$  region which included the Sahara and swathes of Asia, had emissivity increases but the averaged-over-land temperature decreases were small, as there were offsetting emissivity increases in other land areas at the same latitudes. We did not pursue the impact of these emissivity changes further as the CAMEL database is affected by the sta-

713 bility of the MODIS data, and our results below will not include accounting for changes  
714 in land emissivity.

## 715 **7 Results**

716 The trends retrieved in the previous section using simulated radiance trends show  
717 that the retrieval package is working as expected. Here we apply our retrieval to observed  
718 AIRS L1C radiance trends and discuss the retrieved AIRS\_RT geophysical trends to those  
719 computed directly from the ERA5/MERRA2 model fields and AIRS L3/CLIMCAPS L3  
720 products. We will have an expectation that since the simulated radiance trends had no  
721 noise added to them, the uncertainty in the spectral rates was lower than the actual ob-  
722 served spectral uncertainty; this will lead to larger uncertainties and/or errors in our re-  
723 trieval using observed radiance trends.

724 We will make most comparisons against NWP models and L3 products in the con-  
725 text of averages over the descending/night (N) and ascending/day (D) data since the MERRA2  
726 (and GISS) datasets are only available as a D/N average; the reader is referred to the  
727 Appendix where we show a few of the D-N differences. The results are shown in the or-  
728 der of surface/column trends (surface temperature and column water), followed by zonal  
729 averages of the atmospheric temperature and fractional water vapor trends.

### 730 **7.1 Skin Temperature trends**

731 There are typically multiple (window) channels that are sensitive to a surface pres-  
732 sure, meaning the radiances typically have more information content for the surface tem-  
733 perature (assuming the surface emissivity is well known and there are no clouds) rather  
734 than for example air temperature. Figure 7 shows the diurnally averaged day/night (D/N)  
735 surface temperature trends from 6 datasets : AIRS\_RT, AIRS L3, CLIMCAPS L3, ERA5,  
736 MERRA2 and NASA GISTEMP. AIRS\_RT shows an overall global warming of  $+0.021$   
737  $\text{K yr}^{-1}$ ; the cooling trends include the tropical eastern Pacific and south of Greenland  
738 and tropical northern Atlantic. The rest of the datasets also show similar patterns of cool-  
739 ing in the N. Atlantic Ocean, warming over the Arctic and some degree of cooling over  
740 the Antarctic Ice Shelf/Southern Ocean as does AIRS\_RT. The AIRS v7 L3 shows some  
741 cooling over Central Africa and the Amazon not seen in the AIRS\_RT trends, where  
742 one could expect Deep Convective Clouds and possible cloud clearing issues. We also point  
743 out the AIRS L3 product has many missing values off the western coasts of N. and S.  
744 America, due to cloud clearing issues. MERRA2 shows more cooling over C. Africa, and  
745 just like the AIRS v7 data, a lot of cooling near the Antarctic Ice Shelf. Of note here  
746 is that although CLIMCAPS uses MERRA2 as its first guess, their surface temperature  
747 trends are not similar, especially around the Antarctic where MERRA2 shows strong cool-  
748 ing trends. Over the ocean GISS shows similar trends to what AIRS\_RT trends show.  
749 An earlier study of Land Surface Temperatures between 2003-2017 using MODIS Prakash  
750 and Norouzi (2020) shows very similar large daytime cooling trends over parts of cen-  
751 tral and western Indian subcontinent that we see from our retrieval as well as directly  
752 from the BT1231 channel trends; for tiles that straddle both ocean and land the quan-  
753 tile method picks up the hottest observations, which especially during summer are mostly  
754 over the Indian subcontinent. For these reasons we also have confidence in our retrieved  
755 cooling trends over for example daytime continental Central/Eastern Africa, which are  
756 different from the other four day/night datasets.

757

758 The spatial correlations between AIRS\_RT retrieved rates and the various datasets  
759 is shown in Table 2 while the cosine weighted skin temperature trends are shown in Ta-  
760 ble 3. By adding in the uncertainty in the trends for any of the individual models or datasets,

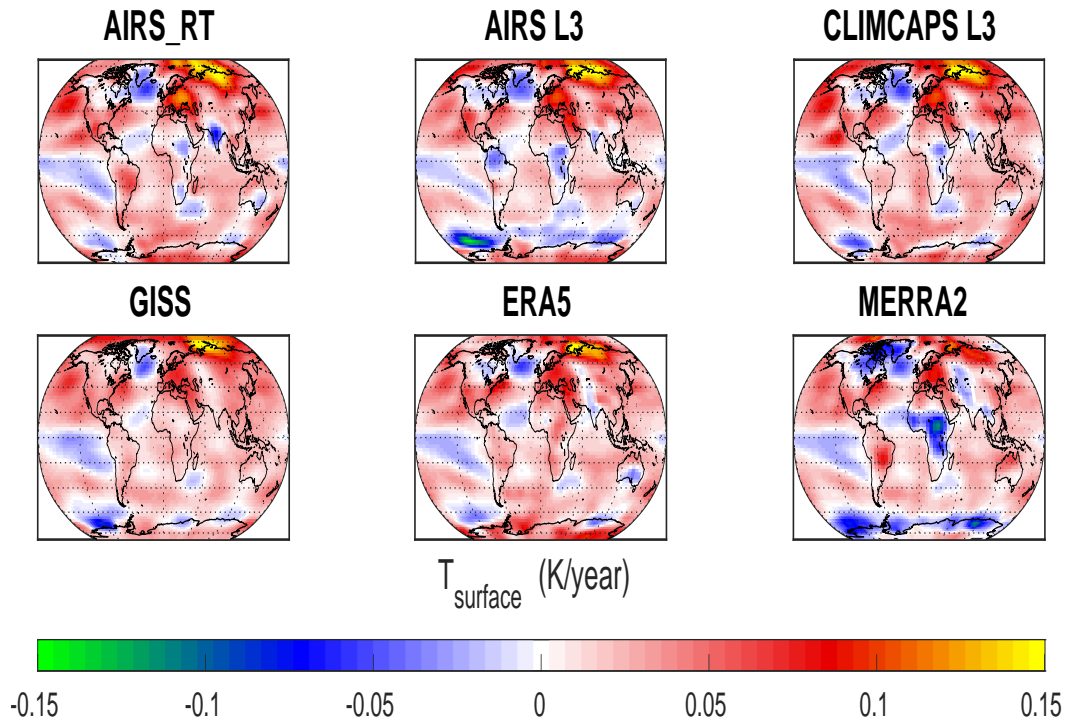


**Figure 7.** Surface temperature trends  $dSKT/dt$  averaged over day and night for AIRS\_RT, and from separately fitting the monthly data in ERA5, MERRA2, AIRS L3, CLIMCAPS L3 and GISS.

761 and then doing the cosine weighting, we estimate uncertainties of about  $\pm 0.015 \text{ K yr}^{-1}$   
 762 for “ALL”; the uncertainties for “OCEAN” are typically about 2/3 of that value, and for  
 763 “LAND” are about 4/3 of that value. We emphasize here that we use all available NWP  
 764 and L3 model data when computing their trends for any grid box, while the AIRS\_RT  
 765 uses only the hottest 10% of “clear” data; Strow and DeSouza-Machado (2020) showed  
 766 that the tropical retrieved surface temperature trends and anomalies over ocean correlated  
 767 very well with those from the ERA-I Sea Surface Temperature dataset.

ERA5	MERRA2	AIRSL3	CLIMCAPSL3	GISS
0.72	0.59	0.80	0.89	0.77

**Table 2.** Correlations of average (nighttime,daytime) retrieved skin temperature trends from AIRS\_RT, versus trends from models/products

768 A notable outlier in this group is the MERRA2 trends, especially over land and  
 769 the Southern Ocean which are noticeable negative (blue) compared to the other datasets;  
 770 the agreement with tropical and mid-latitude oceans is much better. As noted earlier,  
 771 the MERRA2 monthly trends come from a combination day/night dataset that was down-  
 772 loaded, which as seen in Figure 7 consists of trends that are both positive and negative,  
 773 combining to get a closer-to-zero global weighted trend. In addition MERRA2 is the only  
 774 one of the six that (a) does not have the extreme  $+0.15 \text{ K yr}^{-1}$  warming in the north-  
 775 ern polar region and (b) shows a lot of cooling in the Central African area. Using ERA5

SKT trend K yr <sup>-1</sup>	AIRS_RT	AIRS	CLIMCAPS	ERA5	MERRA2	GISS
ALL	0.020	0.017	0.021	0.023	0.011	0.021
TROPICS	0.011	0.011	0.012	0.016	0.010	0.015
MIDLATS	0.029	0.020	0.028	0.026	0.020	0.026
POLAR	0.032	0.028	0.033	0.041	-0.005	0.028
OCEAN	0.019	0.011	0.019	0.017	0.012	0.017
LAND	0.022	0.030	0.024	0.038	0.010	0.030

**Table 3.** Cosine weighted skin temperature trends; uncertainties are on the order of  $\pm 0.015$  K as explained in the text.

776 monthly data, we devised a test similar to the one mentioned in Section 5 to determine  
777 if the differences between MERRA2 and ERA5 surface temperature trends could be due  
778 to the temporal sampling (once for MERRA2 versus eight times for ERA5). For each  
779 month we matched the eight ERA5 timesteps available per month to the tile centers and  
780 then averaged the surface temperatures per month; the ensuing geophysical timeseries  
781 was then trended. The day/night ERA5 average of Figure 7 was compared to these trends;  
782 of note are (a) we did not see the cooling in Africa and near the Antarctic that is seen  
783 in MERRA2 and (b) the main differences between the 1.30 am/1.30 pm average in the  
784 bottom middle (ERA5) panel were over land (all 5 continents); the histograms of the dif-  
785 ferences showed the peak was typically close to 0 K yr<sup>-1</sup>, but the widths over land were  
786 about  $\pm 0.02$  K yr<sup>-1</sup> or less (compared to  $\pm 0.005$  K yr<sup>-1</sup> over ocean). Both AIRS L3  
787 and MERRA2 show cooling in the Southern Ocean; we note that although MERRA2 is  
788 the *a-priori* for CLIMCAPS L3, their trends are different than those from MERRA2; in  
789 fact AIRS\_RT shows the closest correlation to the observational CLIMCAPS L3 trends.  
790 The AIRS L3 trends in the Southern Ocean region could arise because of problems iden-  
791 tifying ice during the L2 retrieval (private communication : Evan Manning (JPL) and  
792 John Blaisdell (NASA GSFC)) though the MERRA2 trends also show significant cool-  
793 ing in that region, where few surface observations from buoys poleward of 60° exist to  
794 help resolve these differences (see for example Figure 10 in Hayden et al. (2018)).

795 Figure 8 shows the zonally averaged total (land+ocean) and ocean only surface tem-  
796 perature trends. Notice how the equator to midlatitude ocean trends are almost linear  
797 for all datasets, with the slope for the northern hemisphere being about double that of  
798 the southern hemisphere (roughly 0.001 K yr<sup>-1</sup> per deg latitude). Again focusing on the  
799 right hand plot, the AIRS L3 trends are negative in the Southern Ocean regions, com-  
800 pared to the other 3 datasets, due to the cooling trends around the Antarctic continent  
801 shown earlier, but then agrees with most of the other datasets over the Antarctic; the MERRA2  
802 trends significantly differ between -90 S and -50 S. MERRA2 and ERA5 also show slightly  
803 smaller warming trends in the Northern Polar, compared to the three AIRS-based datasets.

804

805 We point out that the trends seen in Figure 7 vary noticeably at more local, regional  
806 levels and furthermore this spatial variation can differ between daytime and nighttime,  
807 evident in Figure A1 of Appendix Appendix A, and that the observational sets (AIRS\_RT,  
808 CLIMCAPS L3 and AIRS L3) had larger differences than ERA5. Discussing the possi-  
809 ble causes of this is outside the scope of the paper.

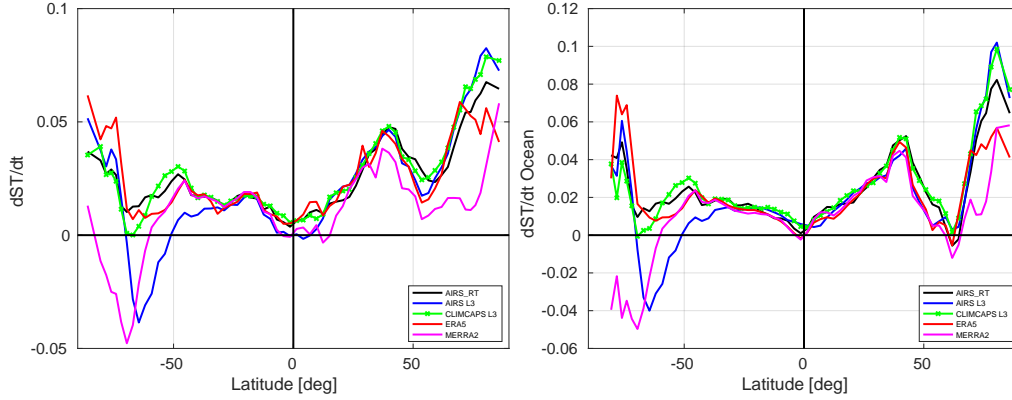


**Figure 8.** Zonally averaged surface temperature trends for (left) sum of ocean and land point and (right) ocean only.

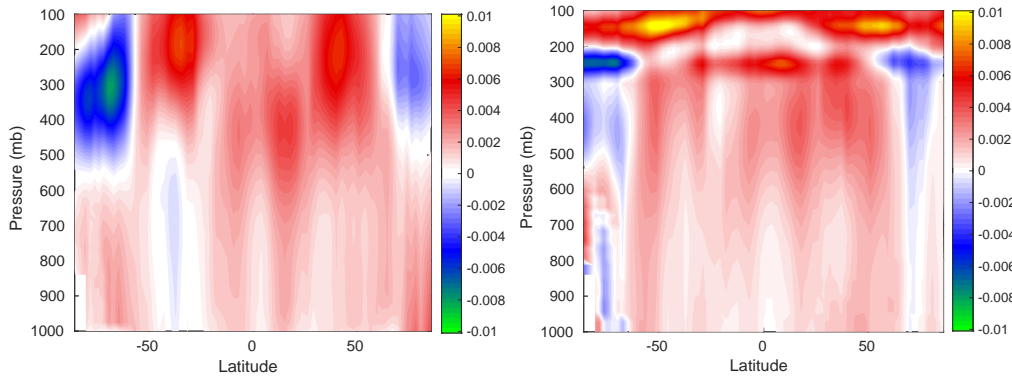


**Figure 9.**  $dWVfrac/dt$  (left) without and (right) with MLS *a-priori* in the upper atmosphere

810

## 7.2 Addition of Microwave Limb Sounder Water Vapor A-priori

811

The Microwave Limb Sounder (MLS), on board NASA’s Aura platform, is designed for sounding of the atmosphere above 300 mb. We computed water vapor trends from the L3 data produced for that instrument (above 300 mb) and used them as an *a-priori* for the AIRS\_RT retrieval.

812

813

814

815

816

Figure 9 shows the retrieved fractional water vapor trends when the *a-priori* trend in the upper atmosphere in the left and right panels were zero, or used MLS trends, respectively. One sees that the additional information brought in by the instrument sensitive to upper troposphere humidity, significantly changes the water vapor sounding especially in the polar region by moving towards the MERRA2 and ERA5 fractional water vapor trends seen in Figure 13. We note that the results shown in this paper use the MLS *a-priori*.

817

818

819

820

821

822

823

## 7.3 Column water vapor trends

824

Column water vapor trends provide an assessment of the water vapor retrieval quality in the lower atmosphere since this is dominated by the layers near the surface. The water vapor information in the lowest layers is best retrieved using the weak water lines

825

826

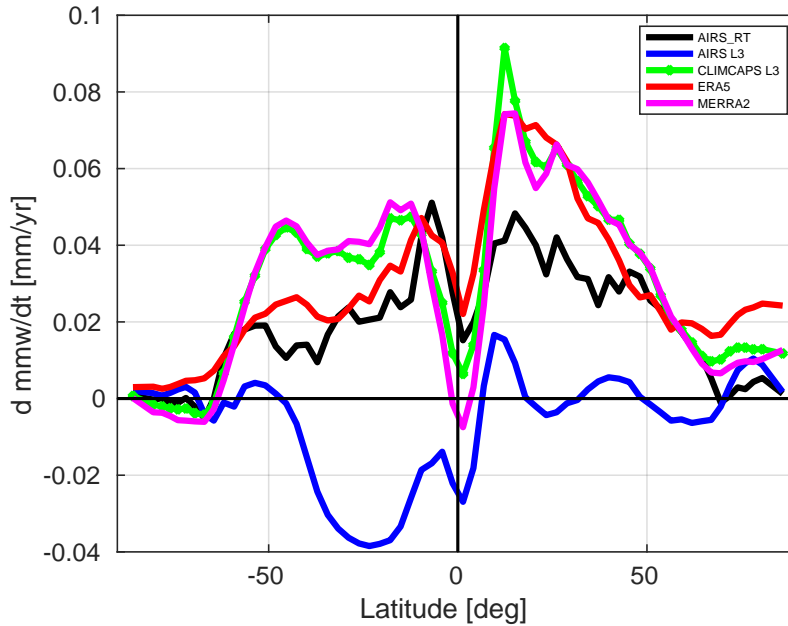


**Figure 10.** Zonally averaged column water vapor trends for AIRS\_RT, AIRS L3, CLIMCAPS L3, ERA5 and MERRA2.

827 in thermal infrared region. This part of the retrieval is significantly complicated by the  
 828 simultaneous presence of nonzero surface temperature, air temperature and water va-  
 829 por jacobians in this spectral region, meaning the AIRS instrument has much reduced  
 830 sensitivity to the water vapor amounts in these lowest layers. In addition the changing  
 831 concentration of very minor gases such as CFC-11 and CFC-12 Strow and DeSouza-Machado  
 832 (2020) are quite evident in the spectral trends, further complicating the water vapor trend  
 833 retrieval for the lowest layers.

834

835 Figure 10 shows the zonally averaged column water vapor trends; not shown are  
 836 the error bars which are on the order of  $\pm 0.005$  mm/year. AIRS\_RT is from our re-  
 837 trievals while the rest are directly from the NWP or L3 model fields. Close examination  
 838 shows the CLIMCAPS L3 column water trend is nearly identical to the MERRA2 trend,  
 839 as is also seen in lower atmosphere water vapor trends shown later in Figure 13. Con-  
 840 versely the column water vapor trends for AIRS L3 are negative in the lower troposphere  
 841 in the midlatitudes and tropics, which is not to be expected given that the surface tem-  
 842 perature trends are positive. AIRS\_RT nominally agrees with ERA5 and MERRA2 in  
 843 the tropics and midlatitudes, but is smaller than either in the northern polar regions.  
 844 A reduced rate for AIRS\_RT is additionally seen in the 0-50 N latitudes, where there  
 845 is a larger fraction of land (for which we do not use the assumption of constant relative  
 846 humidity) compared to the Southern Hemisphere. Screening out the tiles over land slightly  
 847 improves the agreement between reanalysis (ERA5, MERRA2) vs AIRS\_RT column wa-  
 848 ter trends. Examination of the spectral trends in the window region does not shed any  
 849 more insight into the differences, as the observation spectral trends and NWP reconstructed  
 850 trends are very similar and we are fitting the observed trends. The magnitudes and pat-  
 851 terns look similar to the 2005-2021 column water trends shown in Borger et al. (2022),  
 852 which were derived using observations from the Ozone Monitoring Instrument (OMI).  
 853 We point out their 16 year zonally averaged trends look similar to the 20 year ERA5 zon-

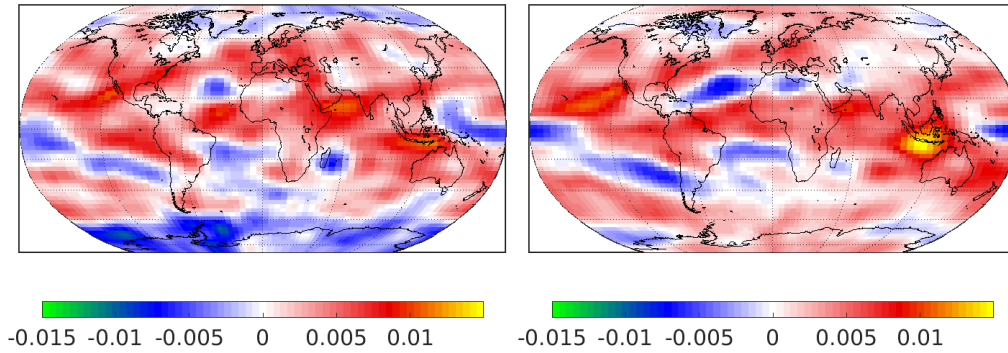


**Figure 11.** The 400 mb fractional water vapor trends for (left) AIRS\_RT and (right) ERA5 show general agreement except in the Southern Polar Regions.

854 ally averaged column water trends between  $-60^{\circ}\text{S}$  and  $-10^{\circ}\text{S}$ , but become almost a fac-  
 855 tor of 2 larger between  $-10^{\circ}\text{S}$  and  $+40^{\circ}\text{N}$ ; the zonally averaged OMI 16 year trends are  
 856 negative in the polar regions. The column water trends are summarized in Table 4.

DATASET mm yr <sup>-1</sup>	OMI 16 years	AIRS_RT 20 years	ERA5 20 years	MERRA2 20 years	AIRS L3 20 years	CLIMCAPS L3 20 years
GLOBAL (cosine average)	0.051	0.021	0.035	0.036	-0.009	0.038
TROPICAL	0.083	0.028	0.047	0.042	-0.015	0.045

**Table 4.** Column water trends based on OMI data (16 years) and AIRS\_RT, ERA5 and MERRA2 (20 years). The units are in mm yr<sup>-1</sup>; the uncertainties are on the order of 0.1 mm yr<sup>-1</sup> for OMI and AIRS\_RT, and half that for ERA5 and MERRA2, and AIRS L3 and CLIMCAPS L3.

857 D/N differences (not shown) for AIRS\_RT were on the order of  $\pm 0.005$  mm yr<sup>-1</sup>  
 858 (with daytime trends being smaller over land), for AIRS L3 were on the order of  $\pm 0.01$   
 859 mm yr<sup>-1</sup> or more (with larger values happening over the daytime tropical oceans), while  
 860 that for ERA5 and CLIMCAPS L3 were typically on the order of  $\pm 0.03$  mm yr<sup>-1</sup> or  
 861 less. Figure 11 shows the 400 mb fractional water vapor trends, with the left panel be-  
 862 ing the AIRS\_RT trends while the right panel is the ERA5 trends. Note that there is  
 863 general agreement except in the Southern Polar region, as also seen later in Figure 13  
 864 in the other two observational L3 datasets (AIRS v3 and CLIMCAPS). This could be  
 865 related to work by Boisvert et al. (2019) who showed decreasing evaporation from the  
 866 Southern Ocean in the 2003-2016 period due to increasing ice cover.

867

#### 868 7.4 Zonal atmospheric temperature and water vapor trends

869

870 Figure 12 shows the zonally averaged atmospheric temperature trends from five of  
 871 the datasets in Figures 7,10 above. In the troposphere the AIRS\_RT retrievals show the  
 872 same general features as the trends from ERA5, though they begin to diverge in the strato-  
 873 sphere and especially above that. In particular AIRS\_RT does not show warming in the



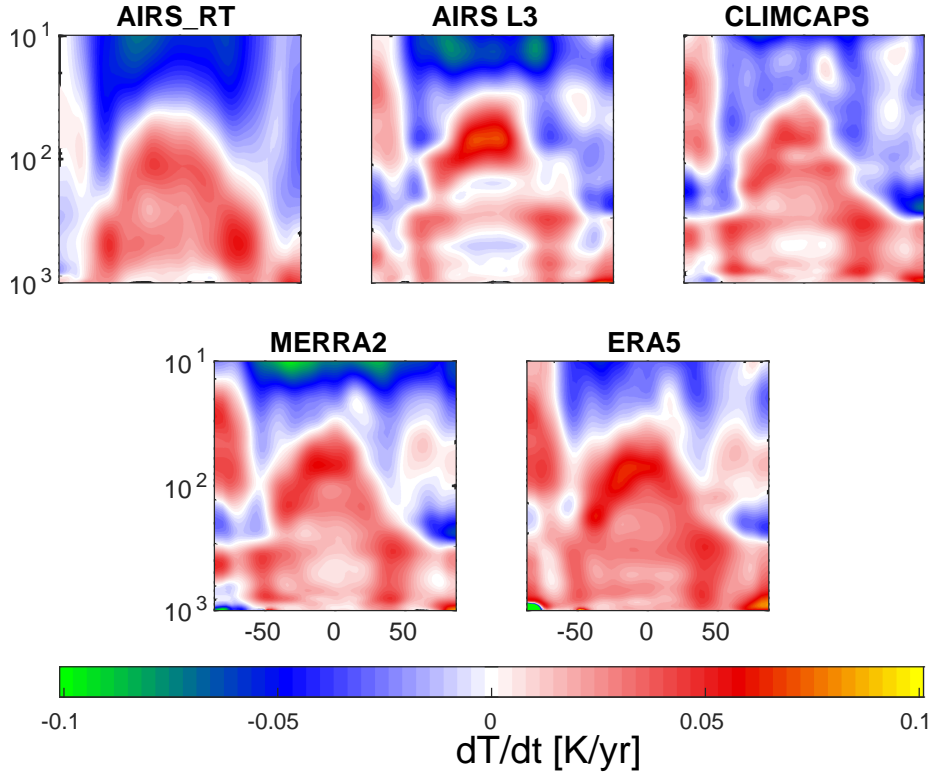


**Figure 12.** Zonally averaged  $dT/dt$  shown in 5 panels. Horizontal axis is latitude while vertical axis is pressure. The  $y$ -limits are between 10 to 1000 mb, on a logarithmic scale.

874 Southern Polar stratosphere; we have separately looked into seasonal trends and noted  
 875 that our retrieved September/October/November temperature trends in the upper at-  
 876 mospheric Southern Polar regions are on the order of  $-0.12\text{K yr}^{-1}$ , possibly leading to  
 877 an overall no net heating/cooling for the annual trends. In addition we point out that  
 878 both our results and AIRS v7 L3 show a hint of cooling over the tropical surfaces. Note  
 879 that CLIMCAPS is initialized by MERRA2, and their temperature trends are quite simi-  
 880 lar. AIRS v7 looks similar to AIRS\_RT except in the tropics where it almost has cool-  
 881 ing in the lower troposphere and much more warming in the lower stratosphere. The cor-  
 882 relations between AIRS\_RT and the [AIRS L3, CLIMCAPS L3, MERRA2, ERA5] tem-  
 883 perature trends of Figure 12 are [0.74,0.65,0.74,0.72] respectively.

884

885 Figure 13 shows the zonally averaged atmospheric fractional water vapor trends  
 886 ( $d/dt \text{ WV}(z,t)/\langle \text{WV}(z,t) \rangle$ ). The five panels are markedly different from one another.  
 887 The AIRS\_RT trends resemble those of ERA5 in the tropical troposphere, though we  
 888 do not have drying in the lower tropical layers. Conversely, the observed trends in the  
 889 Southern Polar (AIRS L3, CLIMCAPS L3 and AIRS\_RT) show drying rather than wet-  
 890 ting, though AIRS\_RT is less than that of CLIMCAPS/MERRA2. AIRS\_RT is an out-  
 891 lier in the upper polar atmosphere trends, as both the signals and the jacobians are close  
 892 to zero. Of some concern is a little bit of drying in the northern polar region, where there  
 893 are low  $\text{H}_2\text{O}$  amounts leading to small jacobians. CLIMCAPS v2 looks quite similar to  
 894 the MERRA2 trends. AIRSv7 shows substantial drying in the lower troposphere, and  
 895 considerable wetting in the upper troposphere, compared to any of the other datasets.  
 896 Spectral closure studies (using the AIRS v7  $\text{H}_2\text{O}$  trend  $\times$  the  $\text{H}_2\text{O}$  jacobians derived above

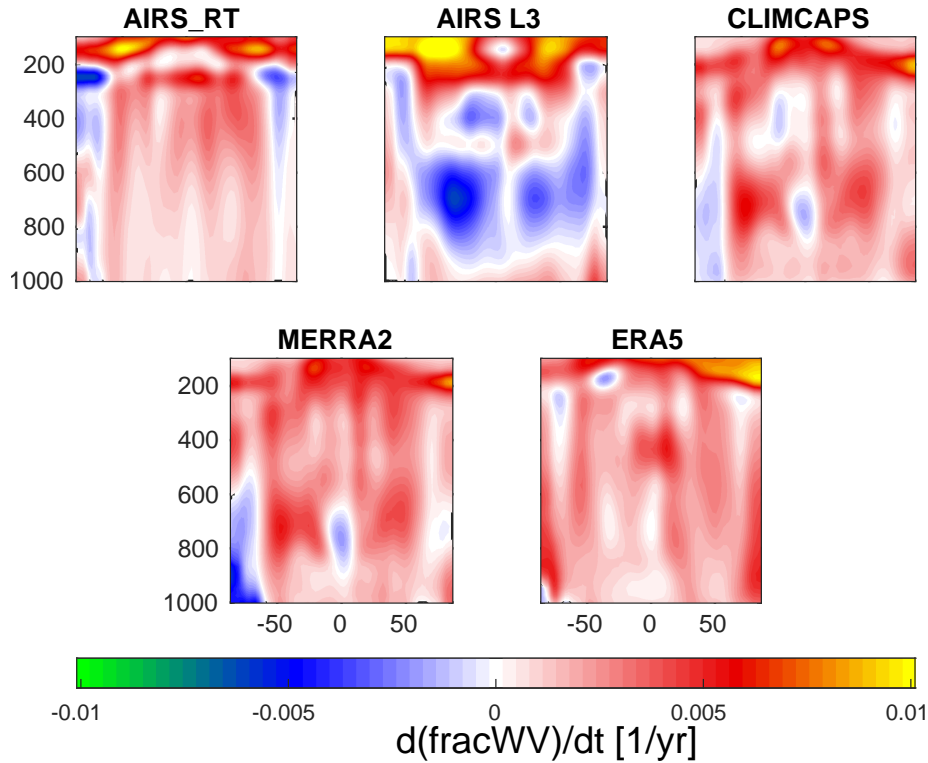


**Figure 13.** Zonally averaged  $d\text{WVfrac}/dt$  shown in 5 panels. Horizontal axis is latitude while vertical axis is pressure. The  $y$ -limits are between 100 to 1000 mb, on a linear scale.

897 from ERA5 average profiles) are not shown here, but differ noticeably from the CCR trends  
 898 from AIRS v7 in the 1300-1600  $\text{cm}^{-1}$  region, indicating there are inadequacies in the AIRS  
 899 V7 water vapor retrievals. The correlations between AIRS\_RT and the [AIRS L3, CLIM-  
 900 CAPS L3, MERRA2, ERA5] fractional water vapor trends of Figure 13 (limited to 100  
 901 mb, 1000 mb) are [0.65,0.24,0.36,0.58] respectively.

## 902 8 Uncertainty

903 The uncertainties for the AIRS v7 geophysical products are impacted by radiance  
 904 noise amplification due to cloud clearing Susskind et al. (2003) and the neural net first  
 905 guess, while state vector errors are estimated based on regressions. CLIMCAPS L2 geo-  
 906 physical products are similarly impacted by cloud clearing noise in the radiances, but  
 907 these are fully propagated together with geophysical error estimates from the MERRA2  
 908 first guess, through the retrieval algorithm which uses Optimal Estimation Smith and  
 909 Barnett (2020). No estimate of uncertainties are available for the monthly L3 products.

910 The uncertainties for the AIRS\_RT trends is much more straightforward : the spec-  
 911 tral uncertainties shown in Figure 4 are used together with the state vector covariance  
 912 matrices to generate the uncertainty matrix using the relevant equations of Optimal Es-  
 913 timation (Rodgers, 2000); we use the diagonal elements for the final uncertainties. Pan-  
 914 els (A) and (C) of Figure 14 shows the zonally averaged (D/N) uncertainties as a func-  
 915 tion of pressure and latitude. Inspection of the radiance trends uncertainties shown in  
 916 the center panel of Figure 4 shows the upper atmosphere temperature sounding region  
 917 ( $650\text{-}700\text{ cm}^{-1}$ ) has much larger uncertainty in the polar regions. The instrument and  
 918 spectroscopy characteristics, coupled with these observational uncertainties, are such that

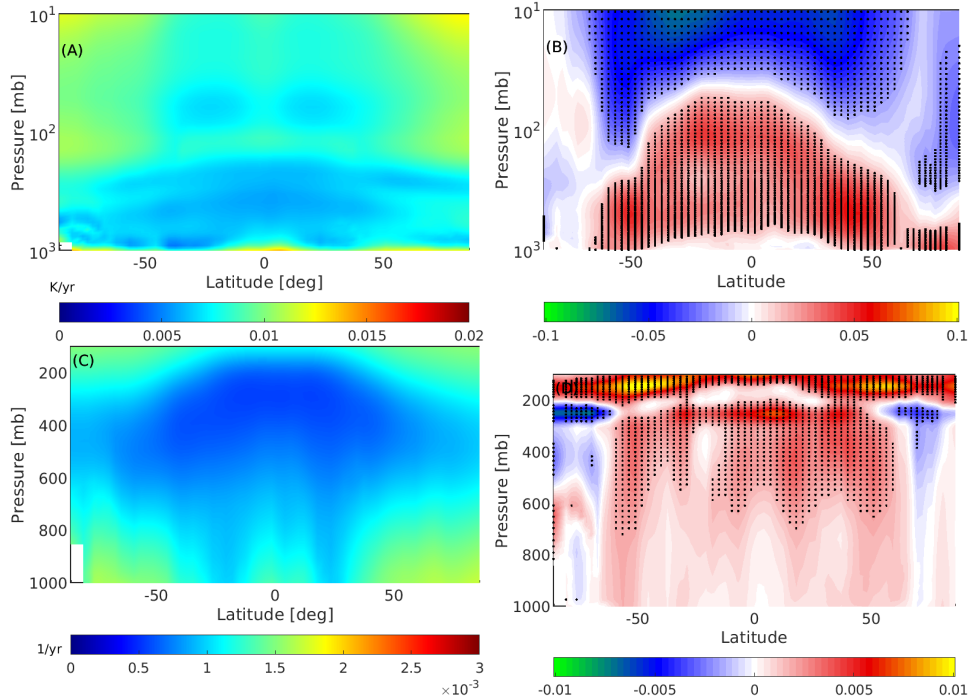


**Figure 14.** Zonally averaged D/N plots of (A) temperature uncertainties in  $\text{K yr}^{-1}$  and (B) temperature trends in  $\text{K yr}^{-1}$  together with null hypothesis. (C) and (D) are the same except for fractional water vapor uncertainty and trends in  $1/\text{year}$ . See text for more detailed explanation.

919 for temperature the smallest errors are in the tropics while the largest errors are in polar  
 920 upper atmosphere, which are the regions below 100 mb where the ERA5 trends differ  
 921 most from AIRS\_RT trends. Similarly for water vapor the larger errors are in the  
 922 lower atmosphere and above about 300 mb; the constant RH assumption and MLS *a-*  
 923 *priori* help alleviate the errors.

924 The *Z-test* confirmed this picture, as seen in panels (B) and (D) of Figure 14, which  
 925 show the temperature and fractional water vapor trends, together with black dots mark-  
 926 ing the (latitude,altitude) points where the trends are larger than the uncertainty in the  
 927 trends, at the 5% significance level. This happens in panel (B) for the temperature trends  
 928 in most of the tropical/mid-latitude free troposphere (and stratosphere) but not at the  
 929 southern polar stratosphere; and in panel (D) for fractional water vapor trends in the  
 930 200-600 mb range, from the Southern Polar region to about +60 N latitude, and some  
 931 spots in the Northern Polar.

932

## 933 9 Discussion

934 In general for surface temperature trends, the disagreements between the six sets  
 935 shown in Figure 7 are over the polar regions and over land (especially over the Amazon  
 936 and Central Africa) and are smallest over tropical and mid-latitude oceans, indicating  
 937 the best agreements, except for slightly larger differences off the western coast of the Amer-  
 938 icas and Africa (which have a prevalence of MBL clouds). The atmospheric temperature  
 939 trends in general agreed except for the upper atmosphere polar regions and in the high  
 940 altitudes (less than about 200 mb). Similarly fractional water vapor trends differed most

941 in the upper atmosphere (200 mb and above) and in the tropical/mid-latitude 600-800  
 942 mb region. A quick glance at Figure 13 shows the former is due to lower sensitivity to  
 943 upper atmosphere water vapor, leading the AIRS\_RT retrievals to have low values while  
 944 the AIRS L2 retrieval is initialized by a neural net; conversely the latter is due to the  
 945 AIRS L3 retrieval being negative while the rest were mainly positive. Similarly the AIRS\_RT  
 946 retrieval differs above the Antarctic continent.

947 In general the observed surface temperature trends from the AIRS\_RT retrievals  
 948 agree with the ERA5 and MERRA2 trends, as well as the NASA GISS trends, except  
 949 in the Southern Antarctic. That is a region where there are few surface observations; for  
 950 retrievals there are competing effects of using ice vs ocean surface emissivity. Overall,  
 951 the AIRS\_RT retrieved surface temperature trends are typically in between ERA5 and  
 952 MERRA2 for land + ocean in all regimes (tropical, midlatitude and polar), though slightly  
 953 larger overall for ocean than the two reanalysis datasets; in general they are closer to the  
 954 ERA5 trends than the MERRA2 trends.

955 Strow et al. (2021) demonstrated that the long- and medium- wave channels of the  
 956 AIRS instrument are radiometrically stable to better than  $0.002\text{-}0.003\text{ K yr}^{-1}$ , which is  
 957 much smaller than the surface and tropospheric temperature trends in the reanalysis mod-  
 958 els, AIRS L3 data and our retrieved trends. A separate analysis of spectral trend un-  
 959 certainties after 05,10,15,20 years (not shown here) show that these uncertainties have  
 960 been steadily decreasing and are now approaching this number, as can be seen in the bot-  
 961 tom left panel of Figure 3. Furthermore, though we cannot guarantee only cloud free scenes  
 962 in our chosen Q0.90 dataset used in this paper, the high correlations between other dataset  
 963 surface trends compared to ours, is a good indication that our results come from mostly  
 964 cloud-free scenes, or scenes whose clouds have negligible impact on our results.

965 The observed zonal temperature trends agree with those from the models and the  
 966 AIRS L3 products, except in the polar regions. Again this could be an issue of using slightly  
 967 incorrect surface emissivity for the AIRS\_RT retrievals. In addition we point out that  
 968 since there is very little water vapor, the temperature jacobians near the surface are quite  
 969 small in magnitude (compared to more humid atmospheres) and so it is difficult to sep-  
 970 arate out the effects of surface temperature trends versus lower atmosphere temperature  
 971 and  $\text{H}_2\text{O}$  trends. The quantile construction used in this paper means that for example  
 972 tiles straddling the subcontinent of India and the ocean will preferentially pick the land  
 973 surface observations for daytime, which could lead to misleading trends on these coastal  
 974 tiles. It is possible to subdivide the  $3^\circ \times 5^\circ$  tiles into for example  $1^\circ \times 1^\circ$  grids and do the  
 975 analysis, but the number of observations per small grid cell would drop, leading to more  
 976 noise in the retrieved trend.

977 The AIRS\_RT retrieved absolute column water trends are equal to/slightly larger  
 978 than ERA5/MERRA2 in the tropics and below both of them in the midlatitudes; AIRS\_RT  
 979 ocean column water trends were slightly smaller than both ERA5 and MERRA2 over  
 980 ocean, and in-between them over land. We note the difficulties we have retrieving  $\text{H}_2\text{O}$   
 981 close to the surface and in the upper atmosphere. This is simply a consequence of the  
 982 sensitivity of the infrared sounder, namely most of the averaging kernels peak in the 300-  
 983 600 mb range. AIRS\_RT column water trends agree with those from ERA5 and MERRA2  
 984 column water trends in the tropics; nevertheless even with expected lowered sensitivity  
 985 to water vapor in the lower altitudes, we were able to retrieve similar column water va-  
 986 por trends to the NWP models both in the tropics and in the mid-latitudes. The dif-  
 987 ferences become more acute in the polar regions since the low average amounts of wa-  
 988 ter vapor mean the water vapor jacobians are very small, as were the observed trends  
 989 in the WV channels. However, we point out that our column water trends, which are both  
 990 quite sensitive to water vapor in the lower atmosphere, are in good agreement with those  
 991 from NWP models.

992 We point out here that our results are relatively robust to changes in the covari-  
 993 ance or Tikonov parameter settings. For instance changing them by factors of two would  
 994 keep the trends about the same, though of course the uncertainties would change.

995 Given the complex numerical algorithms used in both the reanalysis models and  
 996 the AIRS L3 retrievals as well as those in the AIRS\_RT trends, it is difficult to offer pre-  
 997 cise explanations for any of the trends shown above. There are however a few general  
 998 points that can be made. The first is that since infrared instruments are sensitive to the  
 999 300-800 mb region and lose sensitivity outside this, the retrievals from AIRS\_RT and  
 1000 AIRS L3 have difficulties with water vapor in the lower (Planetary Boundary Layer) and  
 1001 upper troposphere/lower stratosphere. One way to mitigate this is to use trended data  
 1002 from external sources in the *a-priori*, while keeping the *a-priori* trends for all other pa-  
 1003 rameters as 0. For example we have shown we can use the MLS data above 300 mb with-  
 1004 out significantly degrading the AIRS\_RT retrieval in the middle and lower atmosphere;  
 1005 conversely the CLIMCAPS retrievals are initialized by MERRA2 and while they can pull  
 1006 out weather signals, their L3 trends are still quite closely tied to the MERRA2 trends.  
 1007 The tropical and mid-latitude ocean surface temperature trends from the numerical mod-  
 1008 els that assimilate data, L3 products and AIRS\_RT are very similar; however they start  
 1009 to show differences where there are few *in-situ* data combined with problems with ice  
 1010 identification (surface emissivity)/cold temperatures which exacerbate the drifting AIRS  
 1011 detector problems Strow et al. (2021), such as the Arctic and Southern Ocean.

## 1012 10 Conclusions

1013 We have described a novel method to obtain global thermodynamic atmospheric  
 1014 climate trends, starting from infrared allsky hyperspectral observations which are then  
 1015 subset for “nominally clear” scenes. Our retrieved trends are derived using trends from  
 1016 well characterized (radiometrically stable) radiances and from zero *a-priori* (except for  
 1017 a constant relative humidity assumption). This makes them much more direct and trace-  
 1018 able than trends from traditional L2 retrieval algorithms, which use complicated *a-priori*  
 1019 information. We also did “radiative closure” tests by running the monthly NWP or L3  
 1020 fields through a radiative transfer model to compare the spectral trends so obtained against  
 1021 the observed spectral trends, which showed the most disagreement in the water vapor  
 1022 sounding regions.

1023 The temperature and water vapor trends retrieved from the “nominally clear” ra-  
 1024 diance trends resemble those computed from monthly ERA5 and MERRA2 reanalysis.  
 1025 The radiative spectral closure helps identify the cause of differences in the geophysical  
 1026 trends, rather than solely attributing them to deficiencies (eg the well known reduced  
 1027 sensitivity to water vapor near the boundary layer and above 200 mb) with our retrieval.  
 1028 For example the AIRS\_RT temperature trends are quite similar to the reanalysis (MERRA2/ERA5)  
 1029 trends, while the water vapor (and/or Relative Humidity) trends are quite different, es-  
 1030 pecially in the lower troposphere and upper troposphere, which is clearly manifest as dif-  
 1031 ferences in the spectral trends in the water vapor sounding region.

1032 The 20 years of AIRS observations were binned into nominal  $3 \times 5$  degree grid boxes  
 1033 covering the planet, with a time step of 16 days, from which anomalies and trends were  
 1034 obtained. To alleviate the reduced sensitivity of hyperspectral sounders to water vapor  
 1035 in the lower atmosphere we used an assumption of 0.01 increase in relative humidity to  
 1036 initialize the *a-priori* lower atmosphere fractional water vapor rates, while we similarly  
 1037 used Microwave Limb Sounder trends as an *a-priori* to address the high altitude water  
 1038 vapor deficiencies caused by lower sensitivity to upper atmosphere water vapor. New or  
 1039 updated time dependent surface emissivity databases may become available in the fu-  
 1040 ture, enabling us to include those effects into Equation 4. Problems in the polar regions  
 1041 and Planetary Boundary Layer water vapor retrievals will be harder to overcome since

1042 there is very little sensitivity to water vapor in these regions, together with fewer obser-  
 1043 vations to compare against, though more work is planned to address both of these.

1044 In this paper we used the 90th quantile (Q0.90) nominally “hottest” observed BT1231  
 1045 data to form a time series over which to obtain radiance trends, after establishing that  
 1046 the spectral trends from this quantile differed by less than about  $\pm 0.0015 \text{ K yr}^{-1}$  from  
 1047 the 50th (or average) quantile. In the future we plan to base the data subset selection  
 1048 on MODIS cloud products (obtained at 1 km resolution compared to the AIRS 15 km  
 1049 resolution). In any case the AIRS L1C Q0.90 spectral trends used for the AIRS\_RT re-  
 1050 sults are very comparable to trends from quality assured binned AIRS CCR data Manning  
 1051 (2022). The quantile method allows us to select which data to use in the trends : we have  
 1052 explored doing the trend retrievals using the cloud fields contained in ERA5, together  
 1053 with the TwoSlab cloud algorithm De Souza-Machado et al. (2018) to compute jacobians  
 1054 when clouds are present, together with trends from the Q0.50 dataset described above.  
 1055 The retrieved geophysical trends resemble those described above in the mid to upper at-  
 1056 mosphere, and differ in the lower atmosphere, but more work is needed on this and is  
 1057 not discussed further. Longwave clear sky flux trends (both outgoing top-of-atmosphere  
 1058 and incoming bottom-of-atmosphere) and climate feedbacks will be discussed in a sep-  
 1059 arate paper.

1060 While the Aqua platform is scheduled to be terminated within the next few years,  
 1061 copies of near identical CrIS instruments are already in orbit, and more will be launched  
 1062 over the next few years, till at least 2040. The Climate Hyperspectral Infrared Radiance  
 1063 Product (CHIRP) Strow et al. (2021) will seamlessly combine the AIRS data between  
 1064 2002-2015 to CrIS data from 2015-2040 to obtain a 40 year observational radiance record  
 1065 over which to study climate. This availability means that AIRS\_RT and future AIRS/CrIS  
 1066 versions, is well positioned to enable climate analysis of geophysical trends for years to  
 1067 come.

## 1068 **Appendix A Day versus Night surface temperature trend differences**

1069 Figure A1 shows the (top) daytime and (middle) nighttime surface temperature  
 1070 trends; from left to right the datasets are (observational) AIRS\_RT, AIRS L3, CLIM-  
 1071 CAPS L3 and (reanalysis) ERA5. In general the AIRS observational datasets show en-  
 1072 hanced daytime cooling over the Indian subcontinent and Central Africa, compared to  
 1073 the ERA5 model; they also show daytime warming trends over continental Europe and  
 1074 central Asia and the Amazon are larger than during the nighttime. With the large ocean  
 1075 heat capacity and smaller land heat capacity, the land is expected to show more of a di-  
 1076 urnal cycle than ocean. ERA5 sees warming over Eastern/Central Africa during daytime  
 1077 while the observational datasets see cooling. Similarly the three observational datasets  
 1078 see more daytime cooling over the Indian sub-continent and south eastern Australia than  
 1079 does ERA5; we omit more detailed analysis in this paper. During the nighttime, the AIRS  
 1080 L3 product has cooling over C. Africa and parts of the Amazon. The day-night differ-  
 1081 ences are seen in the bottom row of the same figure. Note the colorbar is the same for  
 1082 all three rows. The differences are close to zero over the ocean. AIRS\_RT and CLIM-  
 1083 CAPS L3 see more daytime cooling over E. Africa and the Indian subcontinent. Over-  
 1084 all the magnitude of the day - night differences for the observations are larger for the AIRS  
 1085 observational datasets than for ERA5. ERA5 also sees negative differences over Central  
 1086 Asia compared to the AIRS observational datasets, which see positive differences (higher  
 1087 surface temperature trends during the daytime).

1088

1089 The atmospheric temperature and fractional water vapor day-night differences are  
 1090 quite small (compared to the average values) and not shown here; AIRS L3 shows no-

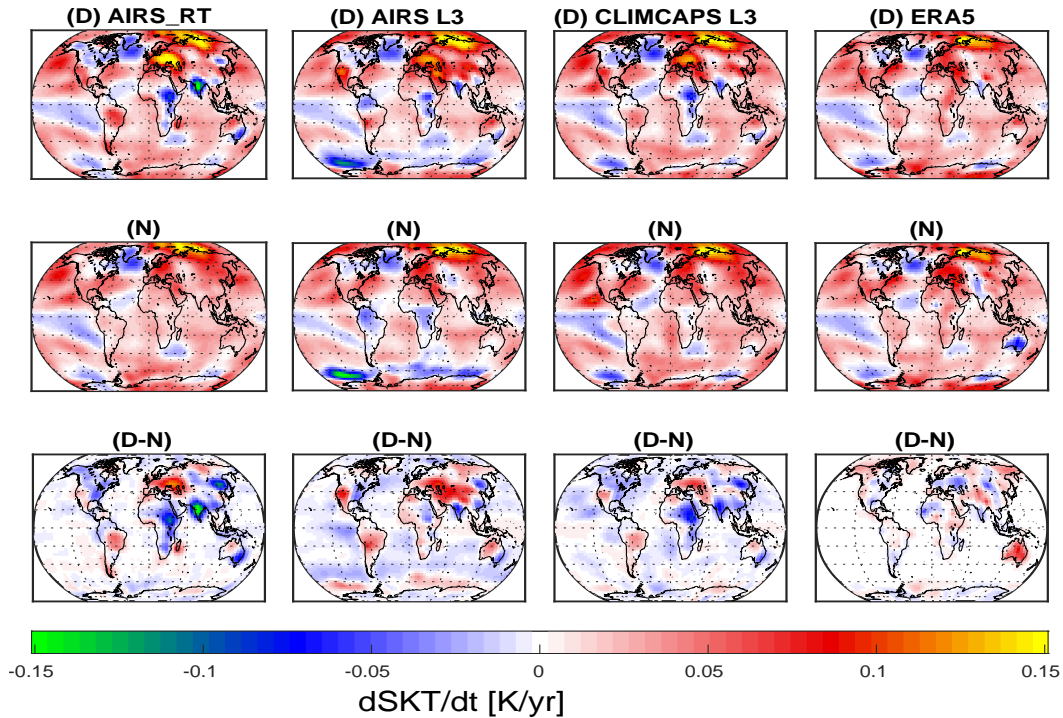


**Figure A1.** Top two rows : The (top) day and (middle) night surface temperature trends for AIRS\_RT, AIRS L3, CLIMCAPS L3 and ERA5. Third row (bottom) is the D-N difference.

1091 ticeable more wetting of the 600-800 mb region during daytime versus nighttime, compared to the other three.  
1092

### 1093 Open Research Section

1094 The AIRS L3 and CLIMCAPS L3 data products, as well as the AIRS L1C radiances are freely available to the public on the NASA servers. MERRA2 and ERA5 and  
1095 GISTEMP model output are also freely available.  
1096

### 1097 Acknowledgments

1098 We gratefully acknowledge the help of H. Motteler, who designed, implemented and ran the AIRS tiling code. C. Hepplewhite helped test the outputs of the tiling code, S.  
1099 Buczkowski worked on bringing down almost all the data used in this study, and made the uniform/clear datasets. Chris Barnet has given helpful comments and general advice regarding retrievals and comparisons to the AIRSv7 and CLIMCAPS datasets. The  
1100 hardware used is part of the UMBC High Performance Computing Facility (HPCF). The facility is supported by the U.S. National Science Foundation through the MRI program  
1101 (grant nos. CNS-0821258, CNS-1228778, OAC-1726023, and CNS-1920079) and the SCREMS program (grant no. DMS-0821311), with additional substantial support from  
1102 the University of Maryland, Baltimore County (UMBC). See [hpcf.umbc.edu](http://hpcf.umbc.edu) for more information on HPCF and the projects using its resources.  
1103  
1104  
1105  
1106  
1107  
1108

1109

**References**

- 2023, G. T. (2005). *GISS Surface Temperature Analysis (GISTEMP), version 4* (Tech. Rep.). data accessed 2023/11/30 at <https://data.giss.nasa.gov/gistemp/>: NASA Goddard Institute for Space Studies.
- Boisvert, L., Vihma, T., & Shie, C.-L. (2019). Evaporation From the Southern Ocean Estimated on the Basis of AIRS Satellite Data. *JGR*, *125*, <https://doi.org/10.1029/2019JD030845>.
- Borbas, E., Hulley, G., Feltz, M., Knuteson, R., & Hook, S. (2018). The Combined ASTER MODIS Emissivity over Land (CAMEL) Part 1: Methodology and High Spectral Resolution Application. *Remote Sens.*, *10*, 643; <https://doi.org/10.3390/rs10040643>.
- Borger, C., Beirle, S., & Wagner, T. (2022). : Analysis of global trends of total column water vapour from multiple years of OMI observations. *Atmos. Chem. Phys.*, *22*, 10603–10621, <https://doi.org/10.5194/acp-22-10603-2022>.
- Clough, S., Shephard, M., Mlawer, E., Delamere, J., Iacono, M. J., Cady-Pereira, K., . . . Brown, P. (2005). Atmospheric radiative transfer modeling : a summary of the AER codes. *J. Quant. Spectrosc. Rad. Trans.*, *91*, 233–244; [doi:10.1016/j.qsrtd.2004.05.058](https://doi.org/10.1016/j.qsrtd.2004.05.058).
- De Souza-Machado, S., Strow, L. L., Motteler, H., & Hannon, S. (2020). kCARTA : A Fast Pseudo Line by Line Radiative Transfer Algorithm with Analytic Jacobians, Fluxes, Non-Local Thermodynamic Equilibrium and Scattering. *Atmos. Meas. Tech.*, *31*, 323–339, <https://doi.org/10.5194/amt-13-323-2020>.
- De Souza-Machado, S., Strow, L. L., Tangborn, A., Huang, X., Chen, X., Liu, X., . . . Yang, Q. (2018). Single-footprint retrievals for AIRS using a fast TwoSlab cloud-representation model and the SARTA all-sky infrared radiative transfer algorithm. *Atmos. Meas. Tech.*, *11*, 529–550, <https://doi.org/10.5194/amt-11-529-2018>.
- Gelaro, R., & Coauthors. (2017). MERRA-2 Overview: The Modern-Era Retrospective Analysis for Research and Applications, Version 2 (MERRA-2). *J. Clim.*, *30*, 5419–5454, [doi: 10.1175/JCLI-D-16-0758.1](https://doi.org/10.1175/JCLI-D-16-0758.1).
- Gordon, I., & Rothman, L. e. a. (2022). The HITRAN 2020 molecular spectroscopic database. *J. Quant. Spectrosc. Rad. Trans.*, *277*, 1–82, <https://doi.org/10.1016/j.jqsrt.2021.107949>.
- Haiden, T., Dahoui, M., Ingleby, B., de Rosnay, P., Prates, C., Kuscü, E., . . . Jones, L. (2018). *Use of in situ surface observations at ECMWF* (No. 834).
- Hersbach, H., Bell, B., Berrisford, P., Hirahara, S., Horányi, A., Muñoz-Sabater, J., . . . Thépaut, J.-N. (2020). The ERA5 Global Reanalysis. *Quart. J. Roy. Meteorol. Soc.*, *146*, 1999–2049, <https://doi.org/10.1002/qj.3803>.
- Huang, X., Chen, X., Fan, X., Kato, S., Loeb, N., Bosilovich, M., . . . Strow, L. (2023). A Synopsis of AIRS Global-Mean Clear-Sky Radiance Trends From 2003 to 2020. *JGR*, *127*, e2022JD037598. <https://doi.org/10.1029/2022JD037598>.
- Irion, F., Kahn, B., Schreier, M., Fetzner, E., Fishbein, E., Fu, D., . . . Yue, Q. (2018). Single-footprint retrievals of temperature, water vapor and cloud properties from AIRS. *Atmos. Meas. Tech.*, *11*(2), <https://doi.org/10.5194/amt-11-971-2018>.
- King, M., Platnick, S., Menzel, P., Ackerman, S., & Hubanks, P. (2013). Spatial and Temporal Distribution of Clouds Observed by MODIS Onboard the Terra and Aqua Satellite. *IEEE*, *51*, 3826–3852, [10.1109/TGRS.2012.2227333](https://doi.org/10.1109/TGRS.2012.2227333).
- Lambert, A., Read, W., Livesey, N., & Fuller, R. (2021). *MLS/Aura Level 3 Monthly Binned Vapor (H2O) Mixing Ratio on Assorted Grids V005* (Tech. Rep.). [https://disc.gsfc.nasa.gov/datasets/ML3MBH20\\_005/summary](https://disc.gsfc.nasa.gov/datasets/ML3MBH20_005/summary): NASA Greenbelt, MD, USA, Goddard Earth Sciences Data and Information Services Center (GES DISC).
- Lenssen, N., Schmidt, G., Hansen, J., Menne, M., Persin, A., Ruedy, R., & Zysse, D.



- 1164 (2019). Improvements in the GISTEMP uncertainty model. *JGR*, *124*(12),  
 1165 6307-6326, doi:10.1029/2018JD029522.
- 1166 Lin, Y., & Oey, L. (2020). Global Trends of Sea Surface Gravity Wave, Wind, and  
 1167 Coastal Wave Setup. *J. Clim.*, *33*, 769–785, <https://doi.org/10.1175/JCLI-D-19-0347.1>.  
 1168
- 1169 Maddy, E., & Barnet, C. (2008). Vertical Resolution Estimates in Ver-  
 1170 sion 5 of AIRS Operational Retrievals. *IEEE*, *66*(8), 2375-2384, DOI  
 1171 10.1109/TGRS.2008.917498.
- 1172 Manning, E. (2022). *Nasa jpl private communication, 4/2022*. (AIRS CCR L3 data)
- 1173 Manning, E., Aumann, H., Broberg, S., Pagano, T., Wilosn, R., Yanovsky, I.,  
 1174 & Strow, L. (2020). *Eos airs 11c data product user guide* (Tech. Rep.).  
 1175 [https://docserver.gesdisc.eosdis.nasa.gov/public/project/AIRS/V6.7\\_L1C\\_Product\\_User\\_Guide.pdf](https://docserver.gesdisc.eosdis.nasa.gov/public/project/AIRS/V6.7_L1C_Product_User_Guide.pdf).  
 1176 NASA.
- 1177 Masuda, K., Takashima, T., & Takayama, Y. (1988). Emissivity of pure and sea wa-  
 1178 ters for the model sea surface in the infrared window regions. *Remote Sensing*  
 1179 *of Environment*, *24*, 313–329.
- 1180 Palchetti, L., Brindley, H., Bantges, R., Buehler, S. A., Camy-Peyret, C., Carli, B.,  
 1181 ... Serio, C. (2020). FORUM: unique far-infrared satellite observations to  
 1182 better understand how Earth radiates energy to space. *Bull.Amer.Met.Soc.*,  
 1183 *101*, <https://doi.org/10.1175/BAMS-D-19-0322.1>.
- 1184 Peters, W., Jacobson, A., Sweeney, C., & Tans, P. (2007). An atmospheric perspec-  
 1185 tive on North American carbon dioxide exchange: CarbonTracker. *Proc. Nat.*  
 1186 *Aca. Sci.*, *104*, 18925-18930, <https://doi.org/10.1073/pnas.0708986104>.
- 1187 Prakash, S., & Norouzi, H. (2020). Land surface temperature variability across In-  
 1188 dia: a remote sensing satellite perspective. *Theor. Appl. Climatol.*, *139*, 773-  
 1189 784, <https://doi.org/10.1007/s00704-019-03010-8>.
- 1190 Raghuraman, S., Paynter, D., V., R., & Menzel, R. H. X. (2023). Green-  
 1191 house Gas Forcing and Climate Feedback Signatures Identified in Hy-  
 1192 perspectral Infrared Satellite Observations. *Geophys. Res. Lett.*, *50*,  
 1193 <https://doi.org/10.1029/2023GL103947>.
- 1194 Rodgers, C. (2000). Inverse Methods for Atmospheric Sounding. In (p. 256 pages).  
 1195 World Scientific, Singapore.
- 1196 Roemer, F., Buehler, S., Brath, M., Kluft, L., & John, V. (2023). Direct observation  
 1197 of Earth’s spectral long-wave feedback parameter. *Nature Geoscience*, *16*, 416-  
 1198 421, <https://doi.org/10.1038/s41561-023-01175-6>.
- 1199 Sherwood, S., Ingram, W., Tshushuma, Y., Satoh, M., Roberts, M., Vidale, P., &  
 1200 O’Gorman, P. (2010). Relative humidity changes in a warmer climate. *J.*  
 1201 *Geophys. Res.*, *115*, <https://doi.org/10.1029/2009JD012585>.
- 1202 Smith, N., & Barnet, C. (2019). Uncertainty Characterization and Propa-  
 1203 gation in the Community Long-Term Infrared Microwave Combined At-  
 1204 mospheric Product System (CLIMCAPS). *Remote Sensing*, *11*, 1227-  
 1205 1251, doi:10.3390/rs11101227.
- 1206 Smith, N., & Barnet, C. (2020). CLIMCAPS observing capability for temperature,  
 1207 moisture, and trace gases from AIRS/AMSU and CrIS/ATMS. *AMT*, *13*,  
 1208 4437–4459, <https://doi.org/10.5194/amt-13-4437-2020>.
- 1209 Smith, N., & Barnet, C. (2023). Practical Implications of CLIMCAPS Cloud  
 1210 Clearing and Derived Quality Metrics. *Earth Space Sci*, *10*, e2023EA002913.  
 1211 <https://doi.org/10.1029/2023EA002913>.
- 1212 Soden, B., & Held, I. (2006). An assessment of climate feedbacks in coupled ocean-  
 1213 atmosphere models. *J. Clim*, *19*, 3354-3360.
- 1214 Strow, L., & DeSouza-Machado, S. (2020). Establishment of AIRS climate-level  
 1215 radiometric stability using radiance anomaly retrievals of minor gases and sea  
 1216 surface temperature. *Atmos. Meas. Tech.*, *13*, <https://doi.org/10.5194/amt-13-4619-2020>.  
 1217
- 1218 Strow, L., Hannon, S., DeSouza-Machado, S., Tobin, D., & Motteler, H. (2003).

- 1219 An overview of the AIRS radiative transfer model. *IEEE Transactions on*  
1220 *Geosciences and Remote Sensing*, 41, 303-313.
- 1221 Strow, L., Hannon, S., Weiler, M., Overoye, K., Gaiser, S., & Aumann, H. (2003).  
1222 Pre-launch spectral calibration of the Atmospheric InfraRed Sounder (AIRS).  
1223 *IEEE Transactions on Geosciences and Remote Sensing*, 41, 274-286.
- 1224 Strow, L., Hepplewhite, C., Motteler, H., Buczkowski, S., & DeSouza-Machado, S.  
1225 (2021). A Climate Hyperspectral Infrared Radiance Product (CHIRP) Com-  
1226 bining the AIRS and CrIS Satellite Sounding Record. *Rem. Sens.*, 13(3),  
1227 <https://doi.org/10.3390/rs13030418>.
- 1228 Susskind, J., Barnet, C., & Blaisdell, J. (2003). Retrieval of atmospheric and sur-  
1229 face parameters from AIRS/AMSU/HSB data under cloudy conditions. *IEEE*  
1230 *Transactions on Geosciences and Remote Sensing*, 41, 390-409.
- 1231 Susskind, J., Blaisdell, J., & Iredell, L. (2014). Improved methodology for surface  
1232 and atmospheric soundings, error estimates, and quality control procedures:  
1233 the Atmospheric Infrared Sounder science team version-6 retrieval algorithm.  
1234 *J. App. Rem. Sens.*, 8(1), 084994 [10.1117/1.JRS.8.084994].
- 1235 Tian, B., E. M., Roman, J., Thrastarson, H., & Fetzer, R., E. ad Monarrexz.  
1236 (2020). *Airs version 7 level 3 product user guide* (Tech. Rep.). Jet  
1237 Propulsion Laboratory, California Institute of Technology. Retrieved from  
1238 [https://docserver.gesdisc.eosdis.nasa.gov/public/project/AIRS/](https://docserver.gesdisc.eosdis.nasa.gov/public/project/AIRS/V7_L3_User_Guide.pdf)  
1239 [V7\\_L3\\_User\\_Guide.pdf](https://docserver.gesdisc.eosdis.nasa.gov/public/project/AIRS/V7_L3_User_Guide.pdf)
- 1240 Whitburn, S., Clarisse, L., Bouilon, M., Safieddine, S., George, M., Dewitte, S.,  
1241 ... Clerbaux, C. (2021). Trends in spectrally resolved outgoing longwave  
1242 radiation from 10 years of satellite measurements. *npj Clim Atmos Sci*, 4,  
1243 48,<https://doi.org/10.1038/s41612-021-00205-7>.
- 1244 Wu, W., Liu, X., Lei, X., L. amd Xiong, Yang, Q., Yue, Q., Zhou, D., & Larar, A.  
1245 (2023). Single field-of-view sounder atmospheric product retrieval algorithm  
1246 : establishing radiometric consistency for hyper-spectral sounder retrievals.  
1247 *AMT*, 16, 4807-4832, <https://doi.org/10.5194/amt-16-4807-2023>.
- 1248 Zhou, D., Larar, A., Liu, X., Smith, W., Strow, L., Yang, P., ... Calbet, X. (2011).  
1249 Global Land Surface Emissivity Retrieved From Satellite Ultraspectral IR  
1250 Measurements. *IEEE Trans. Geosci. Remote Sens.*, 49(4), 1277-1290.